Available online at www.sciencedirect.com
ScienceDirect
Journal of the European Ceramic Society 28 (2008) 407–423
www.elsevier.com/locate/jeurceramsoc

Topotactic growth of α-alumina platelets on 2/1 mullite single crystal surfaces upon thermal decomposition of mullite in dry and wet atmospheres

B. Hildmann *, W. Braue, H. Schneider

German Aerospace Center (DLR), Institute of Materials Research, D-51147 Cologne, Germany

Available online 24 May 2007

Abstract

Annealing experiments of Czochralski-grown 2/1 mullite single crystal coupons, oriented parallel to (1 0 0), (0 1 0), and (0 0 1) were performed in the temperature range 1200–1650 °C for 4–16 h in different atmospheres (dry versus wet air) at normal pressure. Upon thermal decomposition of the Al_2O_3-supersaturated 2/1 mullite, metastable in the two-phase region "mullite plus Al_2O_3", the simultaneous release of alumina and silica gave rise to nucleation and growth of thin, perfect (0 0 · 1) α-alumina platelets which were completely wetted by a glassy phase.

The chemical composition of the initially siliceous glassy phase at the mullite surfaces was shifted to a Na–Mg–Ca bearing alumosilicate composition via uptake of network modifying cations from external impurity sources (kiln furnace material, alumina reaction tube), independent of the nature of the atmosphere. It is this *modified* glassy phase which filled the mullite dissolution paths driven forward by the growing platelets and provided a build-in flux. Growth faces of α-alumina included only special forms of the trigonal point group $\bar{3}2/m$. The habit was very similar to that of sapphire crystals grown from molten fluxes, in agreement with the Wulff shape of undoped α-alumina.

Three different types of α-alumina platelets could be distinguished including (i) type I platelets parallel, (ii) type II platelets perpendicular, and (iii) type III platelets inclined to the mullite surfaces. While type I showed on all mullite substrates investigated, type II platelets did predominantly occur on (0 0 1) and were rarely observed on (1 0 0) and (0 1 0) mullite surfaces. Type III platelets were restricted to (1 0 0) and (0 1 0) mullite surfaces. Platelet types II and III were not independent from each other. Furthermore, for each type of platelets the azimuthal rotation around [0 0 · 1] was restricted to well defined snap-in conditions. A total of 14 symmetrical non-equivalent, topotactic α-alumina/mullite orientation relationships was derived unambiguously by the combined approach of optical microscopy, X-ray diffraction, and focused-ion-beam assisted transmission electron microscopy confirming previous solutions as a sub-assembly group. Possible composition planes characteristic of platelet nucleation on mullite were identified and discussed in terms of coherency of cation sublattices.

Short-term wet annealing of 2/1 mullite at 1650 °C characterized by a low gas flow rate and a water partial pressure of $P_{H_2O} = 0.2P_{total}$ had no effect on the general platelet formation processes and the prevalent orientation relationships as the mullite decomposition rate was distinctly higher than the silica volatilization rate. Topotactic growth of α-alumina (0 0 · 1) platelets influenced by vapor phase impurity doping has been recognized as a widespread phenomenon in numerous other high-temperature investigations of 2/1 mullite single crystals.

Keywords: Mullite; Al_2O_3; Platelets; Impurities; Electron microscopy

1. Introduction

The widespread use of mullite as both, a traditional refractory and a modern high-temperature structural ceramic composite material has encouraged a strong interest in the stability of mullite microstructures in various high-temperature environments.[1,2] The stability range of mullite is limited by a variety of thermal decomposition reaction schemes in time–temperature–P_{total}–P_{H_2O} space.[3,4] In a dry system, decomposition of polycrystalline mullite at high temperatures and low partial oxygen pressures, i.e. in vacuum or reducing atmospheres, is explained by silica volatilization leaving porous α-alumina aggregates.[5–8]

In the present work we compare the decomposition mechanism of 2/1 mullite in dry and wet atmospheres and analyze the crystallography of α-alumina-on-mullite growth on (1 0 0), (0 1 0), and (0 0 1) single crystal sections. The underlying mechanism relies on the metastable nature of the Al_2O_3-supersatured

* Corresponding author. Tel.: +49 2203 601 3554; fax: +49 2203 696480.
E-mail address: Bernd.Hildmann@dlr.de (B. Hildmann).

0955-2219/$ – see front matter © 2007 Elsevier Ltd. All rights reserved.
doi:10.1016/j.jeurceramsoc.2007.03.022

2/1 mullite bulk composition upon annealing at rather moderate temperatures (1200–1650 °C) in the two-phase region "mullite plus α-alumina" of the binary silica-alumina system.[9] Unlike mullite decomposition at higher temperatures silica is not lost via volatilization but retained as a glassy phase quenched from a melt. The net reaction may formally be described by

$$2Al_2O_3{\cdot}SiO_2(s) \rightarrow 2Al_2O_3(s) + SiO_2(s) \quad (1)$$

where s = solid, although it is more complex in fact due to solute effects in the glassy phase (dissolution of mullite, uptake of impurities). Apart from platelet nucleation sites on the mullite lattice, the newly formed α-alumina platelets were completely wetted by the coexisting glassy phase. The nature of the glassy phase and its functionality as build-in flux for enhanced platelet growth has not yet been addressed in the literature and is thoroughly discussed here.

Main focus of this work was on the systematics of the different types of α-alumina platelets, their growth habit and the evaluation of the prevalent α-alumina/mullite orientation relationships. These were determined via the combined approach of optical microscopy (OM), scanning electron microscopy (SEM), X-ray diffraction (XRD), and focused-ion-beam (FIB) assisted transmission electron microscopy (TEM).

Alpha-alumina and mullite feature an intriguing number of lattice planes with close-matching *d*-spacings which reflect structural similarities and immediately suggest some sort of topotactic relationship. For most fine-grained alumina-mullite microstructures however, validation of the three-dimensional orientational and structural resemblance between constituents which Bernal and Mackay[10] considered the precondition for topotaxy may be experimentally impeded[11] thus favoring the use of single crystal over polycrystalline materials.

Mullite, $Al_2[Al_{2+2x}{\cdot}Si_{2-2x}]O_{10-x}$, comprises an oxygen-deficient orthorhombic structure (oxygen vacancies x with $0.17 < x < 0.50$) covering a solid solution range between stoichiometric 3/2 mullite ($3Al_2O_3{\cdot}2SiO_2$, $x = 0.25$) and 2/1 mullite ($2Al_2O_3{\cdot}1SiO_2$, $x = 0.40$). The average mullite structure is described by edge-sharing AlO_6 octahedral chains extending parallel to the crystallographic *c*-axis. The octahedral chains are cross-linked by $(Al,Si)O_4$ tetrahedral double chains.[12–14] Alpha-alumina is rationalized as stacked hcp-type oxygen layers with the Al^{3+} cations occupying 2/3 of the octahedral interstices.[15]

Previous work on α-alumina/mullite orientation relationships was derived from zero-layer Weissenberg patterns collected (i) during in-situ decomposition of mullite at 1750 °C[16] and (ii) from a two phase α-alumina/mullite assemblage solidified from an eutectic melt.[17] In both studies, the specimens were exposed to dry air. Recently orientation relationships derived via electron backscattered diffraction (EBSD) were reported from wet annealed (0 0 1) and (0 1 0) 2/1 mullite single crystal sections.[18] In the present work an extensive data set of α-alumina/mullite orientation relationships will be presented including previous work as a sub-assembly group.

An important issue of the present study concerns the effects of a wet gas atmosphere under low flow rate conditions on both, platelet microstructure and α-alumina-on-mullite orientation relationships as compared to dry annealing experiments. High-temperature corrosion in H_2O-rich combustion atmospheres defines a major concern for implementation of all-oxide ceramic composite materials as a structural material for combustion chambers of stationary gas turbines or future jet engines.[19]

The corrosive effects of high water vapor pressures were studied for a variety of polycrystalline mullite[20–23] and single-crystal mullite materials.[18,24,25] The corrosion mechanism of polycrystalline 3/2 mullite in a wet atmosphere is attributed to the formation of Si- and Al-hydroxides with $Si(OH)_4$ as the dominant volatile species following the simplified net reaction:

$$3Al_2O_3{\cdot}2SiO_2(s) + 4H_2O(g) \rightarrow 3Al_2O_3(s) + 2Si(OH)_4(g) \quad (2)$$

where s = solid, g = gaseous.

The formation of a non-protective, porous alumina layer at the mullite surface is consistent with the linear corrosion kinetics of polycrystalline mullite reported by Fritsch.[22] Previous research[20–23] stated that within the average duration of the wet corrosion experiments (~100 h in the 1300–1500 °C temperature regime) and at high gas velocities, complete loss of silica via $Si(OH)_4$ evaporation was achieved. It is tempting to extrapolate the basic corrosion concept and the data body from the 3/2 to the single crystal 2/1 mullite system. Therefore, the validity of Eq. (2) as the prevalent hot corrosion mechanism for single crystal 2/1 mullite is carefully scrutinized in this study.

2. Experimental procedures

2.1. Single crystal 2/1 mullite starting material

2/1-mullite single crystals employed in this study comprise a chemical composition of 76.7 wt% Al_2O_3 and 23.3 wt% SiO_2 corresponding to $x = 0.385$ in the general structural formula $Al_2[Al_{2+2x}{\cdot}Si_{2-2x}]O_{10-x}$. The crystals were Czochralski-grown following the original procedure developed by Guse and Mateika[26,27] and furnished by the Institute of Crystal Growth (IKZ) Berlin, Germany (courtesy Drs. P. Reiche and S. Uecker). According to the inductively coupled plasma-optical emission spectroscopy (ICP-OES) analysis[28] as-grown 2/1 mullite did not reveal any impurities relevant for this study (below 20 ppm level).

2.2. Mullite surface preparation

As-grown mullite crystals were mounted on goniometer heads to enable precise crystal orientation alignment via high resolution X-ray diffraction methods (HRXRD). Mullite disks of 1 mm thickness and 10 mm diameter oriented parallel to the crystallographic (1 0 0), (0 1 0), and (0 0 1) planes, respectively, were then cut from the aligned, as-grown crystals using an abrasive diamond bladed saw (Accutom-5 with goniometer head holder, Struers, Germany).

The standard polishing procedure employed include polishing to optical quality using (i) 3 μm diamond spray

(Technischer Bedarf Hinkeldey, Germany) and in the final stages (ii) colloidal silica-based suspensions OP-S 0.04 μm (Struers, Germany) as well as FINAL 0.1 μm (Bühler, Germany). The surfaces were then ultrasonically cleaned in isopropyl. All specimens were gem-quality optically clear and devoid of secondary phases or pores. The estimated residual roughness was less than 1 micron. The final orientation of the mullite surfaces were individually confirmed by HRXRD. Residual orientation deviations from (1 0 0), (0 1 0), and (0 0 1) planes were generally smaller than 0.2°, respectively.

2.3. Annealing conditions

Dry annealing experiments of oriented (1 0 0), (0 1 0), and (0 0 1) 2/1 mullite sections were performed at 1400 °C/4 h–16 h in air at normal pressure. Standard exposure time was 4 h. Heating and cooling rates were 20 °C/min. All annealing experiments were performed in the same chamber kiln (model FHT 175/12 supplied by Agni Inc., Aachen, Germany) equipped with $MoSi_2$ heating elements and 50% mullite/50% α-alumina furnace bricks for kiln insulation. In separate experiments, mullite slices were positioned either on a commercial, technical-grade α-alumina type kiln furniture or gem-quality sapphire or wrapped in Pt-foils or placed inside a Pt-crucible.

A series of *wet annealing experiments* were performed with (0 1 0) mullite sections at 1650 °C/8 h, in an O_2/H_2O-gas mixture (80/20) at 100 kPa total gas pressure (courtesy S. Shimada, Hokkaido University, Sapporo, Japan) in an alumina crucible fixed within an alumina reaction tube. The specimens were supported by thin alumina rods. Wet annealing was performed at low flow rate conditions (200 ml/min). The gas velocity was estimated as 3 cm/s which is typical for thermogravimetry under wet conditions.[29]

2.4. Microstructural characterization of mullite/α-alumina orientationships

The surfaces of the heat treated mullite single crystals were analyzed by OM, SEM, XRD, and FIB-assisted TEM. An optical microscope (Aristomet, Leitz Inc., Wetzlar, Germany) was used, and the samples were analyzed both in reflected and transmitted, polarized white light. X-ray analyses were performed by standard and high resolution X-ray diffraction methods (D5000 and D5000HR, Siemens, Germany) in order to determine orientations of the mullite specimens and the newly formed α-alumina platelets.

A scanning electron microscope (LEO Gemini 982, Zeiss Inc., Oberkochen, Germany) equipped with a windowless EDS (Oxford Instruments Inc., Wiesbaden) system was employed for routine microstructural analysis of α-alumina-on-mullite intergrowth.

Thin TEM lamellae of selected α-alumina platelets grown on mullite surfaces were prepared via focused ion beam (FIB) in a single-source FIB (model Strata 205, FEI Inc., Eindhoven, The Netherlands) applying the lift-out technique. A 300 kV TEM/STEM transmission electron microscope (Tecnai F30, FEI Inc., instruments, Eindhoven, The Netherlands) was employed in this study. Selected area diffraction (SAD) patterns were collected across alumina/mullite interfaces tilted to common low-index zone axes. Energy-dispersive (EDS) spectra collected from glassy phases in FIB-derived TEM specimens may exhibit a peak overlap between the Ga Kα and the Na Kα peaks. However, sodium was independently confirmed as a glassy phase constituent via microanalysis of other specimens in a SEM.

2.5. Crystallographic data for analysis of α-alumina/mullite orientation relationships

2/1 mullite crystallizes in space group *Pbam* (55) with lattice parameters $a = 0.75823(6)$ nm, $b = 0.76819(5)$ nm and $c = 0.28865(2)$ nm for the composition of 76.7 wt% Al_2O_3 and 23.3 wt% SiO_2.[30] Alpha-alumina crystallizes in the trigonal space group $R\bar{3}c$ (167) with lattice parameters $a = 0.47587(1)$ nm and $c = 1.29929(3)$ nm (JCPDS card No. 46-1212). The three-axis, three-index notation[31] was applied for hexagonal α-alumina (Miller indices). Nevertheless, for the benefit of immediate distinction between the α-alumina and mullite indices, we formally introduced the dot symbol for planes $(h\,k\cdot l)$ and directions $[u\,v\,\cdot\,w]$ in α-alumina.

Alpha-alumina/mullite orientation relationships were given by pairs of parallel planes $(h\,k\cdot l)//(h\,k\,l)$ and directions $[u\,v\cdot w]//[u\,v\,w]$ with directions lying within the planes. The CARIne Crystallography 3.1 software (http://pros.orange.fr/carine.crystallography/index.html) was employed for visualizing the structural constraints of α-alumina/mullite orientation relationships.

3. Results

3.1. The microstructure of α-alumina-on-mullite intergrowth

Upon the standard annealing procedure at $T \leq 1400$ °C/4 h the formerly smooth mullites surfaces (1 0 0), (0 1 0), and (0 0 1)

Table 1
Type I, II, and III (0 0 · 1) α-alumina platelets grown topotactically on (1 0 0), (0 1 0), and (0 0 1) mullite surfaces, respectively, as compiled from OM, XRD, and TEM observations

Mullite surface $(h\,k\,l)$	Type I platelets (0 0 · 1) α-alumina parallel to $(h\,k\,l)$	Type II platelets (0 0 · 1) α-alumina perpendicular to $(h\,k\,l)$	Type III platelets (0 0 · 1) α-alumina inclined to $(h\,k\,l)$
(0 0 1)	Frequently observed	Frequently observed	Very rarely observed
(0 1 0)	Frequently observed	Rarely observed	Frequently observed
(1 0 0)	Frequently observed	Rarely observed	Frequently observed

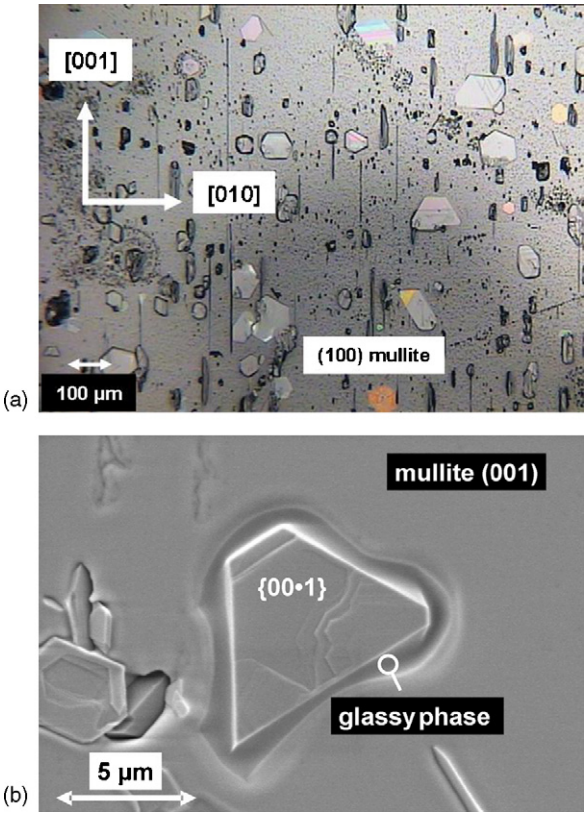

Fig. 1. (a) Typical microstructure of α-alumina-on-mullite intergrowth upon annealing of 2/1 mullite at 1400 °C/4 h (optical micrograph). (b) Type I α-alumina platelet grown on a single crystal (0 0 1) mullite surface (SE image). The platelet is completely wetted by a glassy phase and characterized by truncated pinacoidal faces c $\{0\,0\cdot 1\}$ and rhombohedral faces r $\{0\,1\cdot 2\}$.

were covered by numerous small hexagonal α-alumina $(0\,0\cdot 1)$ platelets (Fig. 1a). Typically the diameter of the platelets was on the order of 30 μm with a thickness of approximately 0.5 μm. Depending on the mullite substrate (Table 1) three different platelet types were identified including (i) *the type I platelet* oriented parallel to the mullite surfaces, (ii) the *type II platelet* oriented perpendicular, and (iii) *the type III platelet* inclined to the mullite surfaces. While type I did occur on all three mullite substrates investigated, type II platelets were predominantly observed on (0 0 1), but rarely on (0 1 0) and (1 0 0) mullite surfaces. Type III platelets were restricted to (0 1 0) and (1 0 0) mullite surfaces.

The growth faces of the α-alumina platelets corresponded to special forms of the trigonal point group $\bar{3}2/m$ dominated by the basic pinacoid c $\{0\,0\cdot 1\}$, see Fig. 1b. These large faces exhibited numerous growth steps. The other growth faces consisted of the first or second order rhombohedral faces r $\{h\,0\cdot l\}$ or d $\{0\,h\cdot l\}$ or the hexagonal bipyramid faces p $\{h\,h\cdot l\}$. No macroscopic hexagonal prisms, neither the m $\{1\,0\cdot 0\}$ nor the a $\{1\,1\cdot 0\}$ faces were observed. Close examination of the platelets showed that each primary platelet was completely surrounded by a thin layer of a glassy phase except for multiple overgrown platelets after annealing experiments exceeding the standard soaking time of 4 h. The growing platelets enforced the formation of narrow mullite dissolution paths filled with glassy phase which extended deeply into the bulk crystal. These microstructural features are discussed here for the first time.

3.1.1. Type I α-alumina platelets

FIB assisted TEM of type I platelet *on* (0 0 1) *mullite* (Fig. 2a) revealed the shallow pool of a Na–Mg–Ca bearing alumosilicate glassy phase (see Section 3.3) separating the platelet from the mullite substrate. The platelet was tilted to a $[1\,0\cdot 0]$ zone axis orientation, mullite orientation was close to $B = [1\,\bar{1}\,0]$. The platelet morphology is defined by pinacoid c $\{0\,0\cdot 1\}$ and rhombohedral r $\{0\,1\cdot 2\}$ faces lacking the macroscopic hexagonal prism face. The composite SAD pattern (Fig. 2b) revealed mutual directions $[0\,0\cdot 1]$//$[0\,0\,1]$ and $[1\,2\cdot 0]$//$[1\,1\,0]$. It should be noted that the reciprocal lattice vectors $0\,\bar{3}\,\cdot\,0$ and $\bar{4}\,\bar{4}\,0$ were parallel, matching in d-spacings within 2% ($d_{0\,\bar{3}\cdot 0} = 0.1374$ nm versus $d_{\bar{4}\,\bar{4}\,0} = 0.1346$ nm). Their role with respect to mutual composition planes is discussed in Section 4.

The low-magnification microstructure of a type I α-alumina platelet *on* (0 1 0) *mullite* is shown in Fig. 3a–e. Contrary to the other mullite specimens annealed in dry furnace atmosphere this

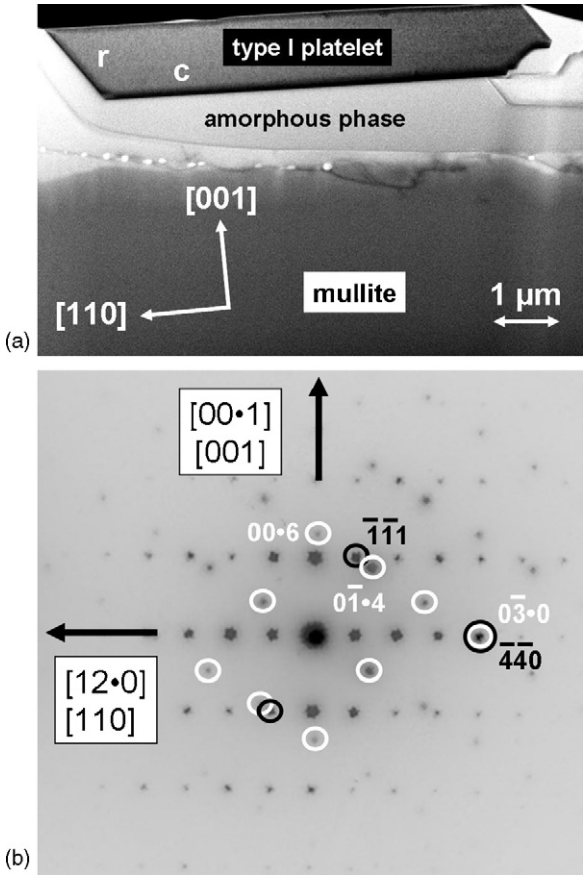

Fig. 2. (a) FIB lamellae displaying a type I $(0\,0\cdot 1)$ α-alumina platelet ($B = [1\,0\cdot 0]$) grown on a (0 0 1) mullite surface (TEM, bright field (BF)). Platelet morphology is defined by pinacoidal c and rhombohedral r faces. (b) Composite SAD pattern of type I α-alumina platelet ($B = [1\,0\cdot 0]$) on (0 0 1) mullite ($B = [1\,\bar{1}\,\cdot\,0]$), printed in inverse contrast. Mutual directions include $[0\,0\cdot 1]$//$[0\,0\,1]$ and $[1\,2\cdot 0]$//$[1\,1\,0]$. Note perfect match of $0\,\bar{3}\,\cdot\,0$ and $\bar{4}\,\bar{4}\,0$ reciprocal lattice vectors, α-alumina/mullite reflections highlighted by white/black circles, respectively.

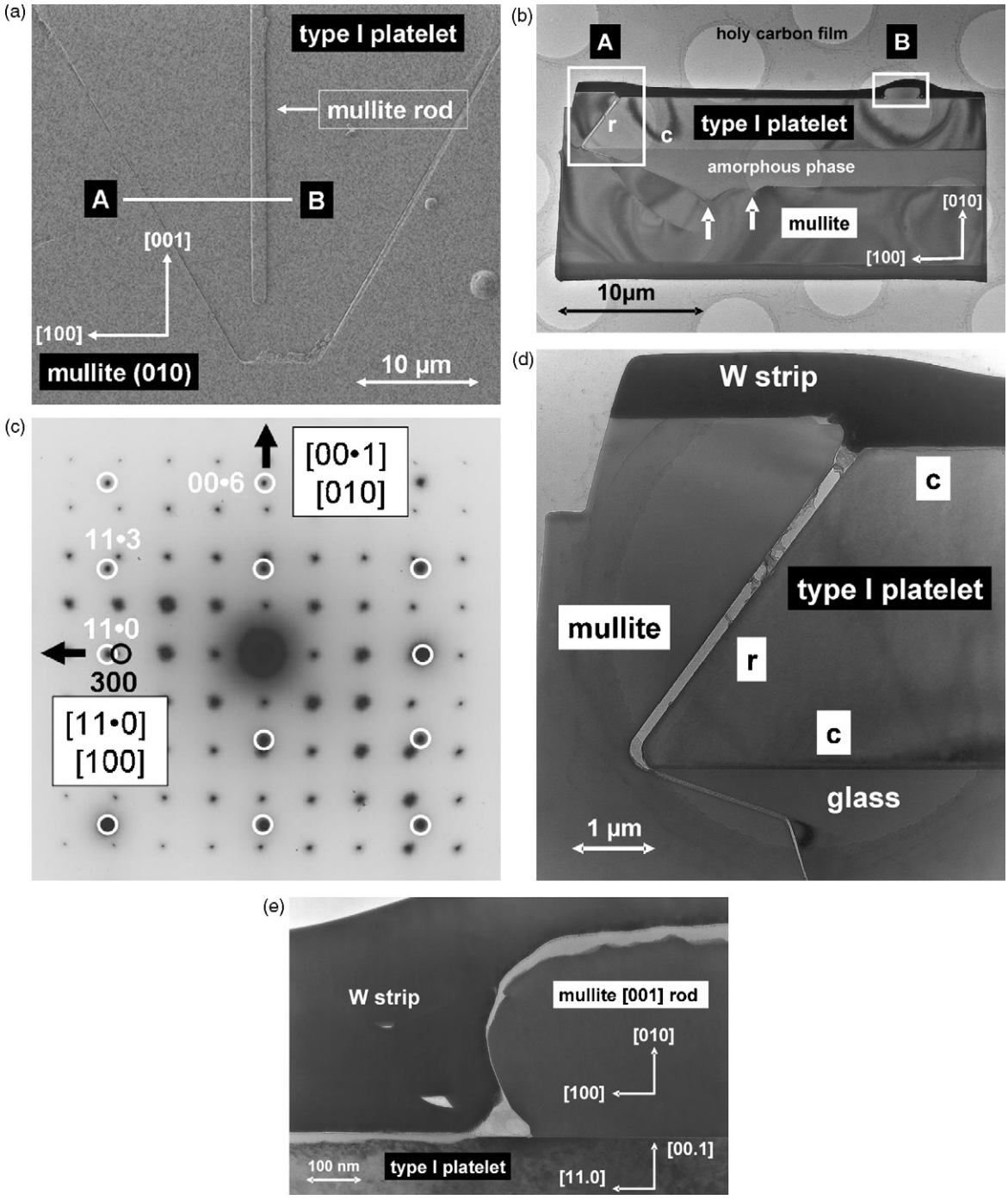

Fig. 3. (a) Formation of a type I α-alumina platelet on (0 1 0) mullite followed by epitaxial growth of a secondary mullite [0 0 1] rod on the α-alumina platelet (wet annealing, SE image, plane view). FIB section AB is displayed in subpart (b). (b) FIB section revealing type I α-alumina platelet on (0 1 0) mullite (TEM, BF) upon wet annealing. Platelet morphology is defined by pinacoidal c $\{0\,0\cdot 1\}$ and rhombohedral r $\{0\,1\cdot 2\}$ faces. Note cusp formation (marked by arrows) at the mullite/glass interface due to local dissolution of mullite. For close-ups on regions A and B see subparts (d) and (e). (c) Composite SAD pattern of type I α-alumina platelet ($B = [\bar{1}\,1\,\cdot\,0]$) on (0 1 0) mullite ($B = [0\,0\,1]$) taken from region A. Mutual directions include $[0\,0\cdot 1]//[0\,1\,0]$ and $[1\,1\cdot 0]//[1\,0\,0]$, α-alumina/mullite reflections highlighted by white/black circles, respectively. (d) De-wetting along a thin surface connected glass layer adjacent to type I α-alumina platelet. Note that the glassy phase underneath the platelet is left unaffected by wet corrosion (TEM, BF). (e) Secondary mullite [0 0 1] rod grown on top of a type I α-alumina platelet (TEM, BF).

(0 1 0) substrate was annealed at 1650 °C/8 h under moderate wet conditions. The high water vapor partial pressure imposed corrosive damage on the alumosilicate glassy phase, but had no further effect on platelet formation and mutual α-alumina/mullite orientation relationships, as discussed in Section 3.4 and shown in Fig. 3d and e. Platelet orientation in Fig. 3b is parallel to $[\bar{1}\,1\cdot 0]$ identifying the rhombohedral face r $(0\,1\cdot 2)$ as the terminating face. Mullite orientation was exactly parallel to [0 0 1] (cf. Fig. 3b and c). Upon the 8 h mullite annealing experiment local dissolution of the mullite surface was still effective giving rise to cusp formation (highlighted by arrows in Fig. 3b) along the mullite/glass interface.

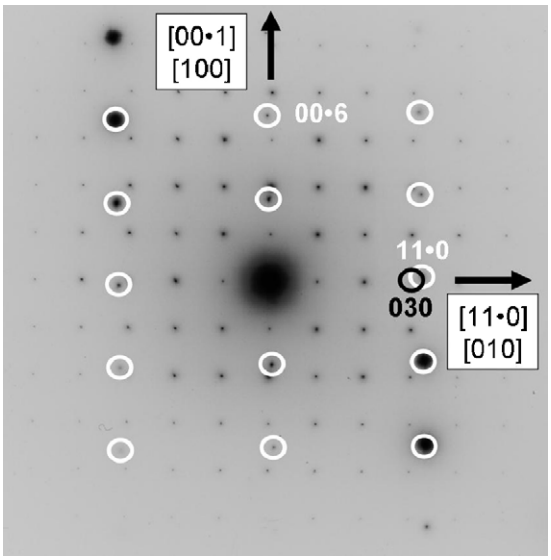

Fig. 4. Composite SAD pattern of type I α-alumina platelet ($B = [\bar{1}\,1\,\cdot\,0]$) grown on a (1 0 0) mullite substrate ($B = [0\,0\,1]$). Mutual directions include [0 0·1]//[1 0 0] and [1 1·0]//[0 1 0], α-alumina/mullite reflections are highlighted by white/black circles, respectively.

The composite SAD pattern shown in Fig. 3c was collected from region A in Fig. 3b. With the zone axes orientation $[\bar{1}\,1{\cdot}0]//[0\,0\,1]$ it revealed two more pairs of mutual directions: [0 0·1]//[0 1 0], [1 1·0]//[1 0 0]. Interestingly, the type I α-alumina platelet itself (Fig. 3b and e) served as a convenient nucleation site for a secondary mullite [0 0 1] rod. Reprecipitation of mullite on a type I α-alumina platelet from the vapor phase is interpreted as indirect evidence that our wet annealing experiment was indeed following local steady-state conditions.

The composite SAD pattern of a type I α-alumina platelet *on* (1 0 0) *mullite* is displayed in Fig. 4 indicating mutual directions [0 0·1]//[1 0 0], [1 1·0]//[0 1 0] and the zone axes $[\bar{1}\,1\,\cdot\,0]//[0\,0\,1]$.

3.1.2. Type II α-alumina platelets

The microstructure of a type II α-alumina platelet *on* (0 0 1) *mullite* is displayed in Fig. 5a–d. The platelet nucleated at the surface and grew about six microns into the bulk mullite crystal. The platelet was tilted parallel to [1 0·0] while mullite was close to $[1\,\bar{1}\,0]$. The terminating face at the upper end of the α-alumina platelet was nearly invisible due to sputter effects from the Pt overlay strip, but the significance of the rhombohedron *r* (0 1·2) as a growth face at the bottom part of the platelet was obvious from Fig. 5c. The central part of the composite SAD pattern is shown in Fig. 5d. Analysis of the full composite SAD pattern yielded (0 0·1)//(1 1 0) with $[1\,0{\cdot}0]//[1\,\bar{1}\,0]$.

The type II α-alumina platelet grown perpendicular *on* (0 1 0) *mullite* were rarely observed. One example is shown in Fig. 6a (plane view) and Fig. 6b (cross section). The platelet was sandwiched by amorphous layers of the same chemical composition as discussed above. Here, the hexagonal bipyramid *p* (1 1·3) was the terminating face of the platelet which was in fact approximated by steps of small hexagonal bipyramids faces (2 2·3) and (2 2·9). Zone axis orientation was $B = [\bar{1}\,1\,\cdot\,0]$. As the type II configuration was achieved by a 90° rotation of the type I α-alumina platelet, (1 1·0) was now parallel with (0 1 0) mullite in the SAD pattern (Fig. 6c). Note that the hexagonal prism *a* {1 1·0} was not developed as macroscopic growth form. Three pairs of mutual directions could be identified: [1 1·0]//[0 1 0], [0 0·1]//[1 0 0], and the zone axes $[\bar{1}\,1{\cdot}0]//[0\,0\,1]$.

3.1.3. Type III α-alumina platelets

The type III platelet *on* (0 1 0) *mullite*, displayed in Fig. 7a, was tilted by an angle of 72° with respect to the (0 1 0) mullite surface. Except for this tilting angle type III platelets held the same characteristics as type I and II platelets in terms of platelet morphology and composition of the embedding amorphous phase. By coincidence the FIB section unfolded a possible α-alumina nucleation site (region A, Fig. 7a) close to the mullite surface where mullite and α-alumina were directly bonded in the early stages of α-alumina nucleation, devoid of an interfacial amorphous layer. The macroscopic hexagonal bipyramid face *p* (2 2·3) was close to being level with the (0 1 0) mullite plane, in agreement with the X-ray diffraction data (Table 2). The composite SAD pattern collected from region A (Fig. 7b) revealed again three pairs of mutual directions including $[0\,0{\cdot}1]//[\bar{3}\,1\,0]$, [1 1·0]//[1 3 0] and the zone axis $[\bar{1}\,1\,\cdot\,0]//[0\,0\,1]$. With mutual lattice planes 1 1·0//1 3 0 a reasonably good match was achieved ($d_{1\,1{\cdot}0} = 0.238$ nm versus $d_{1\,3\,0} = 0.2427$ nm).

3.2. Topotactic orientation relationships of (0 0·1) α-alumina platelets on (1 0 0), (0 1 0), and (0 0 1) mullite surfaces

This paragraph comprises the synopsis of structural data derived from OM and XRD with the TEM data discussed in the previous section which all merge in the prevalent orientation relationships as listed in Table 2. OM and XRD investigations were essential to this study as they assured access to a large number of α-alumina platelets.

3.2.1. Type I α-alumina platelets

Analyzing the (1 0 0), (0 1 0), and (0 0 1) mullite disks in transmitted, polarized, white light, the orientation of the α-alumina platelets parallel to the surface became evident. Upon rotation under crossed nicols the extinction positions were exclusively determined by mullite because the platelets were optically isotrop when viewed parallel to their *c*-axes. The glassy phase had no effect on the extinction behaviour of the mullite substrate. No stress birefringence was observed in mullite at platelet–mullite interfaces.

As an important result of this study, the azimutual rotation of type I α-alumina platelets around [0 0·1] was not arbitrary but restricted to unique "snap-in conditions" defined by specific mullite directions in the substrate surfaces being parallel to the a_1-axes, as shown in Fig. 8a. For the (0 0 1) mullite substrate these included [1 0 0], [0 1 0], [1 1 0], $[1\,\bar{1}\,0]$, [1 3 0], $[1\,\bar{3}\,0]$, [3 1 0], $[3\,\bar{1}\,0]$ (i.e. eight orientation states of which five are symmetrical non-equivalent) while on the (1 0 0) and

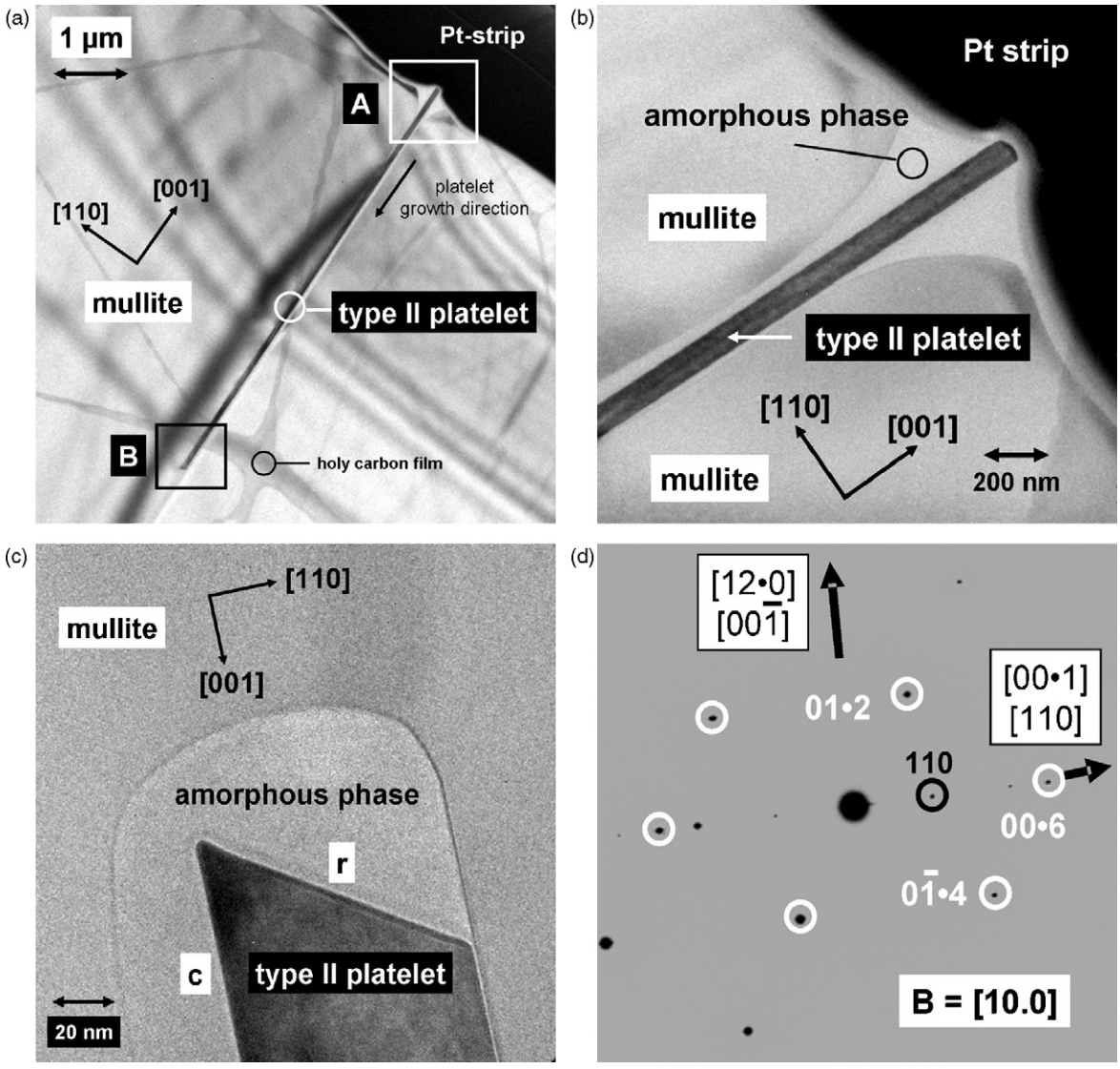

Fig. 5. (a) FIB section across a type II (0 0· 1) α-alumina platelet grown on the (0 0 1) mullite surface (TEM, BF). Platelet growth direction is indicated by arrow. See (b) and (c) for details from regions A and B, respectively. (b) Close-up of the near-surface region A of type II α-alumina platelet in (a). (c) Close up of region B in (a) revealing the bottom part of the type II α-alumina platelet in [1 0·0] zone axis orientation while still embedded in amorphous phase (TEM, BF). Terminating faces include pinacoidal *c* and rhombohedral *r* faces. (d) Composite SAD pattern of type II α-alumina platelet (a–c, $B = [1\,0{\cdot}0]$) on (0 0 1) mullite. Mullite is close to the [1 $\bar{1}$ 0] zone axis orientation, α-alumina/mullite reflections highlighted by white/black circles, respectively.

(0 1 0) mullite sections the [0 1 0], [0 0 1] and [1 0 0], [0 0 1] directions were observed (i.e. a total two orientation states), respectively.

For optical microscopy the hexagonal axes a_1 and a_2 were assumed to be oriented *parallel* to the morphological edges of the α-alumina platelets. This first choice of axes corresponds to a platelet morphology characterized by rhombohedral faces $r\,\{h\,0{\cdot}l\}$ truncated by the dominating pinacoidal faces $\{0\,0{\cdot}1\}$. It is obvious from α-alumina symmetry that for those platelets exhibiting truncated hexagonal bipyramidal faces $p\,\{h\,h{\cdot}l\}$ the hexagonal axes a_1 and a_2 are *perpendicular* to the morphological edges. As the platelets were extremely thin, it was not possible via optical microscopy to discriminate unambiguously between terminating rhombohedral and bipyramidal faces and thus, to assign the correct choice of axes a_1, a_2 to the individual type I platelets. The two alternative orientations are related to each other by 90° (or 30°) rotations corresponding to the second and third non-equivalent symmetry direction in the trigonal/hexagonal system. Since all orientation states observed could be arranged in individual pairs with their axes related by 90° rotation (Fig. 8a), the choice of axes had no consequence on the orientation relationships, as both options yield symmetry equivalent results. Therefore, the orientation relationships listed in Table 2 are independent of the choice of axes.

Two different orientation states A und B of α-alumina platelets could be distinguished for a (1 0 0) mullite substrate (Fig. 8b) with the a_1-axis being either parallel to [0 0 1] (case A) or [0 1 0] (case B) of mullite. The corresponding orientation relationships comprised (i) case A: [1 0·0]//[0 0 1] with (0 0·1)//(1 0 0) and (ii) case B: [1 0·0]//[0 1 0] with (0 0·1)//(1 0 0) which is in perfect agreement with the early XRD data by Guse and Saalfeld.[17]

Table 2
Topotactic orientation relationships of (0 0·1) α-alumina platelets on mullite as derived from optical microscopy, X-ray diffraction, and electron microscopy from this study and previous work[16–18]

Orientation relationships (this work)	Data source (this work)	Previous work
(0 0·1)||**(1 0 0) plus [1 0·0]**|||**[0 0 1]**	Type I on (1 0 0) OM & XRD	**(0 0·1)**||**(1 0 0) plus [1 0·0]**|||**[0 0 1]**[17]
(0 0·1)||**(1 0 0) plus [1 0·0]**|||**[0 1 0]** (0 0·1)||(1 0 0) plus [1 1·0]|||[0 1 0] * (0 0·1)||(1 0 0) plus [1 1·0]|||[0 1 0] *	Type I on (1 0 0) OM & XRD Type I on (1 0 0) TEM Type II on (0 1 0) TEM	**(0 0·1)**||**(1 0 0) plus [1 0·0]**|||**[0 1 0]**[17]
(0 0·1)||**(0 1 0) plus [1 0·0]**|||**[0 0 1]**	Type I on (0 1 0) OM & XRD	**(0 0·1)**||**(0 1 0) plus [1 0·0]**|||**[0 0 1]**[18]
(0 0·1)||**(0 1 0) plus [0 1·0]**|||**[1 0 0]** (0 0·1)||(0 1 0) plus [1 1·0]|||[1 0 0] *	Type I on (0 1 0) OM & XRD Type I on (0 1 0) TEM	**(0 0·1)**||**(0 1 0) plus [0 1·0]**|||**[1 0 0]**[18]
(0 0·1)||**(0 0 1) plus [1 0·0]**|||**[1 0 0]**	Type I on (0 0 1) OM & XRD	
(0 0·1)||**(0 0 1) plus [1 0·0]**|||**[0 1 0]**	Type I on (0 0 1) OM & XRD	
(0 0·1)||**(0 0 1) plus [1 0·0]**|||**[1 1 0]** (0 0·1)||(0 0 1) plus [0 1·0]|||[1 1 0] *	Type I on (0 0 1) OM & XRD Type I on (0 0 1) TEM	
(0 0·1)||**(0 0 1) plus [1 0·0]**|||**[1 3 0]**	Type I on (0 0 1) OM & XRD	
(0 0·1)||**(0 0 1) plus [1 0·0]**|||**[3 1 0]**	Type I on (0 0 1) OM & XRD	
(0 0·1)||**(1 1 0) plus** [1 $\bar{1}$ · 0]|||**[0 0 1]** and/or [0 1·0]|||[0 0 1] ▲ (0 0·1)||(1 1 0) plus [1 2·0]|||[0 0 1] *	Type II on (0 0 1) OM & XRD Type II on (0 0 1) TEM	**(0 0·1)**||**(1 1 0) plus** [1 $\bar{1}$ · 0]|||**[0 0 1]**[16]
(0 0·1)||**(1 3 0) plus** [1 $\bar{1}$ · 0]|||**[0 0 1]** and/or [0 1·0]|||[0 0 1] ▲ (0 0·1)||($\bar{1}$ 3 0) plus [$\bar{1}$ 1 · 0]|||[0 0 1] *	Type II on (0 0 1) OM & XRD Type III on (1 0 0) TEM	**(0 0·1)**||**(1 3 0) plus** [1 $\bar{1}$ · 0]|||**[0 0 1]**[16]
(0 0·1)||**(3 1 0) plus** [1 $\bar{1}$ · 0]|||**[0 0 1]** and/or [0 1·0]|||[0 0 1] ▲ (0 0·1)||($\bar{3}$ 1 0) plus [$\bar{1}$ 1 · 0]|||[0 0 1] *	Type II on (0 0 1) OM & XRD Type III on (0 1 0) TEM	**(0 0·1)**||**(3 1 0) plus** [1 $\bar{1}$ · 0]|||**[0 0 1]**[16]
(0 0·1)||**(2 3 0) plus** [1 $\bar{1}$ · 0]|||**[0 0 1]** and/or [0 1·0]|||[0 0 1] ▲	Type II on (0 0 1) OM & XRD	
(0 0·1)||**(3 2 0) plus** [1 $\bar{1}$ · 0]|||**[0 0 1]** and/or [0 1·0]|||[0 0 1] ▲	Type II on (0 0 1) OM & XRD	

*: symmety equivalent relations to the bold notations (preferred).
▲: additional, symmetry independent orientation relationships deduced from XRD observations, however, not confirmed by TEM.

For type I platelets on all mullite substrates, the XRD reflections 0 0·6 and 0 0·1 2 were recorded with the highest intensities of all corundum reflections, although at randomly oriented powder samples these are very weak. Thus, standard XRD clearly proved that the (0 0·1) planes of the platelets are oriented parallel to the (1 0 0), (0 1 0), and (0 0 1) mullite surfaces, in agreement with Table 1.

3.2.2. Type II α-alumina platelets

Orientations involving type II platelets were easily accessed by optical microscopy. For a mullite disk rotated into the extinction position the platelets appeared as bright stripes in transmitted polarized white light since their optical axes are oriented perpendicular to the viewing direction. As for type I platelets the glassy phase sandwiching type II platelets did not affect mullite extinction. Most important, no stress birefringence was observed at the mullite/glass interfaces caused by type II platelets.

In Fig. 8c type II platelet orientations on (0 0 1) mullite were determined via trace analysis by achieving a close match between the calculated and observed mutual angles between low-index tautozonal (*h k* 0) mullite planes. The analysis yielded (0 0·1) being parallel to {1 1 0}, {1 3 0}, {3 1 0}, {2 3 0} and {3 2 0} mullite planes, in agreement with the TEM results, see Section 3.1.2. These orientation relationships represent five symmetrical non-equivalent orientation states.

The optical findings were corroborated by the XRD data. At (0 0 1) mullite surfaces, reflections of type *h* 0·0 and *h h*·0 occurred almost exclusively, i.e. 1 1·0, 3 0·0, 2 2·0 and 3 3·0 were very strong. Except for traces of the reflections 1 1·3 and 1 1·6 all other α-alumina reflections were absent including the reflection 4 1·0. Consequently, these α-alumina platelets were predominantly oriented perpendicular to (0 0 1) of mullite, and, furthermore, their (1 0·0) and (1 1·0) planes were parallel to (0 0 1), i.e. in terms of directions [1 $\bar{1}$ · 0]//[0 0 1] and [0 1·0]//[0 0 1], respectively. As XRD did not allow an unambiguous correlation between (0 0·1)//(*h k* 0) and either one of these pairs of directions, both options were listed in Table 2 in bold and with the diamond symbol (▲), respectively. In contrast, at (1 0 0) and (0 1 0) mullite surfaces, reflections of type *h* 0·0 and *h h*·0 were absent or negligibly small. Consequently at these surfaces type II platelets occurred very rarely or even not at all, in agreement with Table 1.

3.2.3. Type III α-alumina platelets

Due to their inclined nature type III platelets could not be discriminated positively from type II platelets via optical microscopy. Therefore, they were characterized by XRD supplementary to the FIB assisted TEM discussed in Section 3.2. With the Bragg-Brentano geometry, reflecting planes must be parallel to the mullite surface within the vertical divergence (<5°) of the X-ray beam.

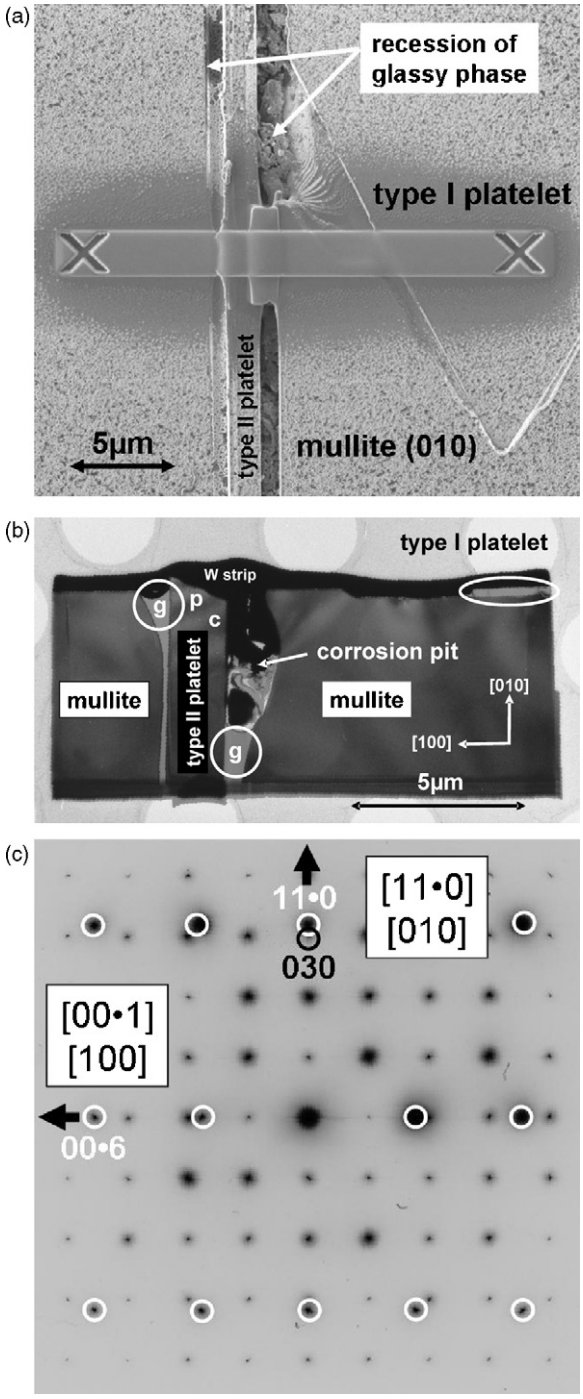

Fig. 6. (a) Plane view of a type II α-alumina platelet grown on a (0 1 0) mullite substrate (SE image, wet annealing). See (b) for corresponding FIB section. (b) FIB section across a type II α-alumina platelets on a (0 1 0) mullite substrate (TEM, BF). Note corrosive attack of the alumosilicate glassy phase (denoted "g") during annealing of (0 1 0) mullite under wet conditions. Terminating faces include pinacoidal *c* and hexagonal bipyramidal *p* faces. (c) Composite SAD pattern of type II α-alumina platelet ($B = [\bar{1}\,1\,\cdot\,0]$) grown on (0 1 0) mullite ($B = [0\,0\,1]$). Mutual directions include [1 1·0]//[0 1 0] and [0 0·1]//[1 0 0], α-alumina/mullite reflections are highlighted by white/black circles, respectively.

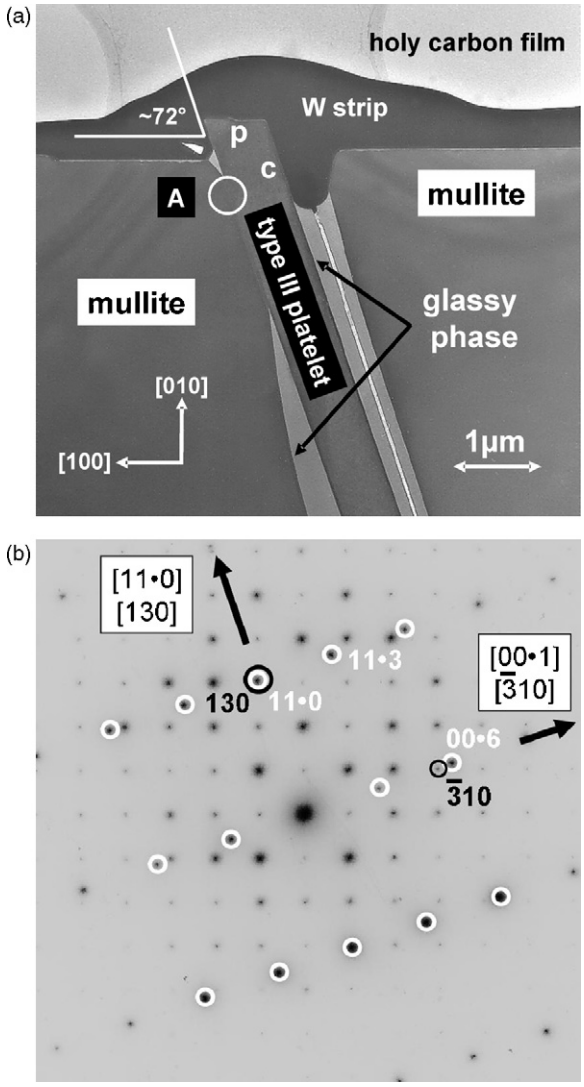

Fig. 7. (a) FIB section across a type III α-alumina platelet tilted by an angle of approximately 72° with respect to (0 1 0) mullite surface (wet annealing, TEM, BF). Region A defines a possible α-alumina nucleation site on mullite close to the surface. Platelet is bound by pinacoidal *c* and hexagonal bipyramidal *p* faces. (b) Composite SAD pattern of type III α-alumina platelet ($B = [1\,\bar{1}\,\cdot\,0]$) on (0 1 0) mullite ($B = [0\,0\,1]$). Mutual directions include [0 0·1]//[$\bar{3}$ 1 0] and [1 1·0]//[1 3 0]. Note perfect match of (1 1·0) and (1 3 0) reciprocal lattice vectors, α-alumina/mullite reflections highlighted by white/black circles, respectively.

At (1 0 0) and (0 1 0) mullite surfaces reflections of the type hh·l and h0·l with $l \neq 0$ were recorded very strong, i.e. the reflections 1 1·3, 2 2·6, 1 1·6, 2 0·2, 1 2·5, and 1 0·4. All other reflections were absent or negligibly small. The inclination angles of these strongly reflecting α-alumina planes with respect to the (0 0·1) plane were found to be consistent with the angles observed between the tautozonal mullite planes (1 3 0), (3 1 0), (1 1 0), (2 3 0), and (3 2 0) – which were parallel to the (0 0·1) plane of a type II platelet – and the (0 1 0) and (1 0 0) mullite surfaces, respectively. Consequently, any extension of type II platelets on (0 0 1) mullite would intersect the (0 1 0) and (1 0 0) mullite surfaces at oblique angles where they would show as type III platelets.

This is illustrated in Fig. 8d confirming that the type III platelet from Fig. 7a tilted ~72° with respect to (0 1 0) mullite is consistent with a type II platelet on (0 0 1) mullite with (0 0·1)//(3 $\bar{1}$ 0). Thus, orientation variants derived from type III

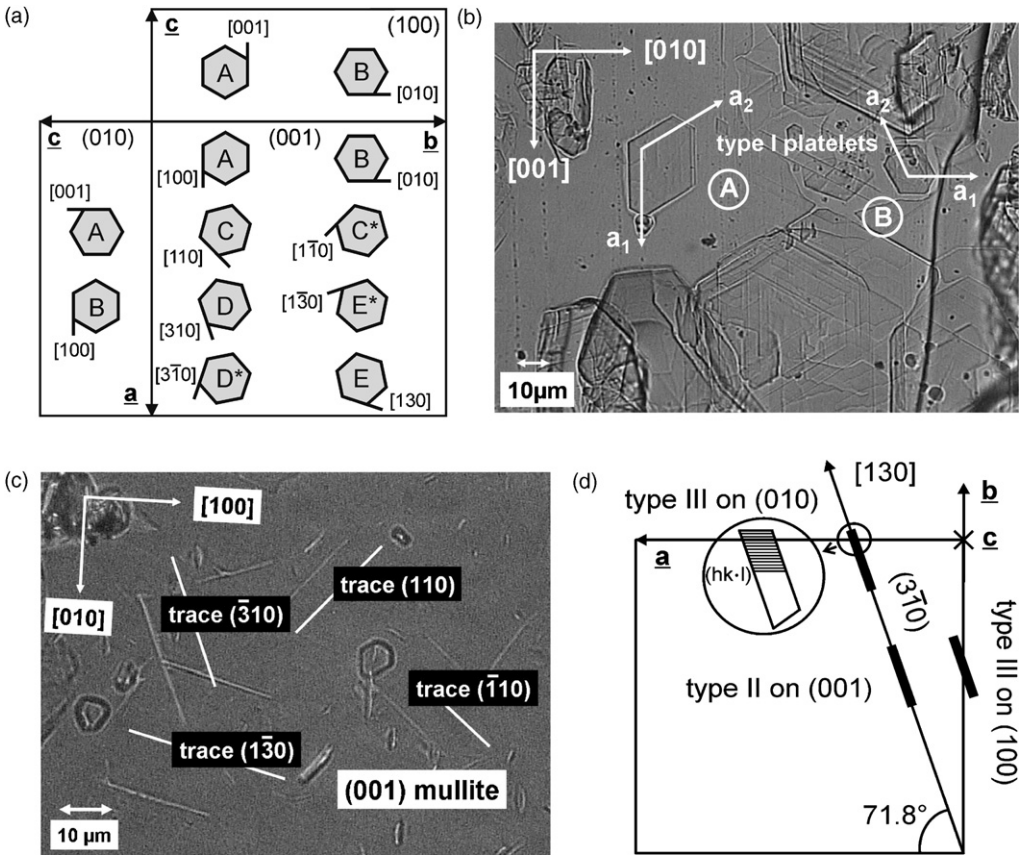

Fig. 8. (a) Schematic rationalizing the limited azimutual rotation of type I (0 0·1) α-alumina platelets with the a_1-axis being parallel to low-index directions [u v w] on the (1 0 0), (0 1 0), and (0 0 1) mullite surfaces ("snap-in conditions"). Symbols A to E denote the different orientation states of the platelets, pairs C–C*, D–D*, and E–E* are interrelated through the mirror symmetry in mullite. On all three mullite surfaces the platelets form pairs with their a_1-axes mutually perpendicular to each other. On (0 0 1) these pairs were arranged horizontally in the drawing. (b) Type I (0 0·1) α-alumina platelets grown on a (1 0 0) mullite surface (optical micrograph, reflection mode). Two different orientation relationships with the α-alumina a_1-axis being parallel to either the mullite [0 0 1] (case A) or [0 1 0] direction (case B) are displayed. (c) Mullite (0 0 1) surface holding both, type I and II (0 0·1) α-alumina platelets (optical micrograph, transmission mode, crossed polars). Alignment of the (0 0·1) plane from edge-on type II α-alumina platelets with respect to the mullite planes (highlighted by white lines) has been derived from trace analysis. (d) Schematic of Fig. 7a showing that type III α-alumina platelets on (1 0 0) and (0 1 0) planes can be rationalized via simple extension of type II α-alumina platelets on (0 0 1). Inset highlights the significance of lattice planes (*h k·l*) oriented nearly parallel to the substrate surface for satisfying reflection conditions in the XRD goniometer with Bragg-Brentano geometry.

platelets have to be consistent with those observed for type II on the other mullite surfaces. The very rare occurrence of type III α-alumina platelets on (0 0 1) mullite (Table 1) is a direct consequence of the sporadic appearance of type II platelets on (0 1 0) and (1 0 0) mullite, respectively.

Table 2 summarizes the complete set of topotactial α-alumina on mullite orientation relationships as derived from OM, XRD, SEM, and TEM data of this study as compared to previous work.[16–18] The literature data were transferred to our orientation relationship notation. In our work the nature of the atmosphere was found to have no effect on α-alumina/mullite orientation relationships. This finding is corroborated by the fact that our data body comprised the published orientation relationships derived from both, dry *and* wet annealing as a subassembly group. For each individual solution the data source and the corresponding characterization technique are given. Note that type III platelets were not listed in Table 2 as independent orientation relationships because type II and III are correlated to each other. Orientation relationships are given in the conventional notation (*h k·l*)//(*h k l*) plus [*u v* · *w*]//[*u v w*] with directions lying in the corresponding planes. The bold notations of the orientation relationships are preferred. Asterisks (*) indicate symmetric equivalent relations to the bold notations. Solutions highlighted by diamond symbols (▲) are additional, independent orientation relationships deduced from XRD observations, however, without confirmation by TEM. They have to be considered due to an orientation ambiguity in the integral XRD pattern of type II platelets (see Section 3.2.2). These five relations were not included in the total of 14 symmetrical non-equivalent orientation relationships of α-alumina platelets on mullite.

3.3. The effects of external impurity sources on the composition of the glassy phase embedding the α-alumina platelets

Small probe microanalysis of the glassy phase revealed an alumosilicate composition of 87.5 wt% SiO_2, 12.5 wt% Al_2O_3 (normalized average), with minor amounts of sodium, magnesium and calcium totalling approximately 5 wt%. Sodium concentrations exceeded those of magnesium and calcium. It

should be noted that within small deviations the same nominal glass composition was obtained from all mullite substrates investigated. Thus, the initially silica-rich glassy phase acted as a preferred sink for impurities during annealing of 2/1 mullite.

It has been a crucial issue of this research to identify the possible impurity sources affecting the glassy phase. *Intrinsic impurity sources* could be ruled out, as the sodium content of as-grown 2/1 mullite crystals was far below the detection limit of ICP-OES analysis. Obviously impurities were related to *external impurity sources*. Polishing agents were ruled out likewise as annealing experiments with very clean ion-etched mullite surfaces showed no effect on the bulk composition of the glassy phase in comparison with the standard polished and ultrasonic-cleaned mullite surfaces. Impurity sources were therefore limited to (i) the kiln furniture material and the refractories utilized for furnace wall isolation (*dry annealing*) and (ii) alumina sample holder tubes (*wet annealing*).

Notably mullite surfaces facing upward to the furnace atmosphere during annealing behaved differently as compared to those facing downward to the kiln furniture material. Similar top/bottom effects were confirmed in a large variety of dedicated annealing experiments performed within the same furnace. Our findings can be summarized as follows:

- α-alumina nucleation was observed after a first 1400 °C/4 h annealing experiment only for bottom mullite surfaces lying more or less flat on the α-alumina kiln furniture. Full contact with the kiln furniture material was not required, a small gap between constituents was sufficient indicating that impurity transport was achieved via the vapor phase. A high density of α-alumina platelets was formed in close contact with the kiln furniture whereas at some distance platelets with high crystalline perfection were formed.
- No α-alumina formation was observed for mullite surfaces facing upwards. Instead, these surfaces were covered with numerous small droplets (see below).
- Turning the former top mullite surface (devoid of α-alumina platelets) over and placing it on the kiln furniture for a second 1400 °C/4 h annealing experiment resulted in the common platelet formation on the new bottom side.
- No α-alumina platelets were observed on the bottom mullite surface when the α-alumina kiln furniture was replaced by a gem-quality polished sapphire disk.
- A mullite slice placed inside a Pt-crucible was found devoid of α-alumina platelets on the surfaces. Several hexagonal Pt platelets were formed via condensation from the vapor phase. Droplets were present on the upper mullite surface.
- Annealing the mullite substrate at a lower temperature, e.g. 1200 °C/4 h produced few clusters of tiny α-alumina platelets at the bottom surface only. Platelet density increased for the 1300 °C/4 h, annealing condition. Heavy overgrowth of stacked α-alumina platelets was observed when the 1400 °C/4 h annealing experiment was extended to 12 h or the specimen exposed to 1600 °C/4 h.
- Surface roughness was not a critical parameter for α-alumina nucleation.

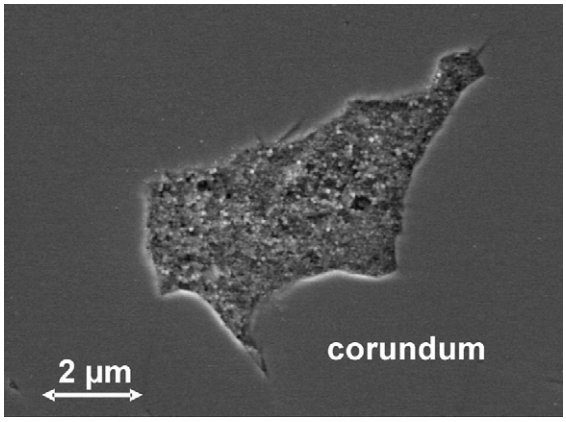

Fig. 9. Chipped surface region of the technical grade α-alumina kiln furniture material exposing a fine-grained Na, Mg- and Ca-bearing siliceous secondary phase at a triple grain pocket (SE-image).

Microstructural analysis showed that the kiln furniture was not single-phase α-alumina. The surface of the kiln furniture tiles exhibited numerous chipped areas which exposed a fine-grained crystalline Na, Mg, and Ca bearing siliceous secondary phase (confirmed by EDS) as shown in Fig. 9. ICP-analysis of the kiln furnace material yielded 280 ppm Na, 1040 ppm Mg, 250 ppm Ca and 596 ppm Si emphasizing that the kiln furnace material was indeed the primary impurity source active during annealing of 2/1 mullite. The chamber kiln insulation made of 50% α-alumina–50% mullite bricks has to be considered as another potential impurity source but this material has not been analyzed in more detail.

The droplets (Fig. 10a–c) were identified as condensation products from the furnace atmosphere upon cool-down from annealing in both, dry and wet atmospheres. They appeared on any surface offered to the furnace atmosphere while their numbers are correlated with the exposure time.

Droplets may show on both, the top and bottom surfaces of mullite slices but occured together with α-alumina platelets only on the bottom surfaces, in close contact with the kiln furniture material. The droplets exhibited average particle sizes between 5 and 20 μm and consisted of amorphous phase quenched from a melt. Their spherical shape indicated a low wettability with the mullite substrate along with high surface tension of the melt during deposition. While droplets may hold various secondary phases they were devoid of α-alumina nuclei (Fig. 10b). Despite their similar chemical composition with the glassy phase upon prolonged exposure times, droplets must not be confused with true α-alumina nucleation sites as it has been stated in other work.[25]

Notably the droplets deposited on mullite surfaces caused substantial reactive wetting (Fig. 10a) offering the chance to study 2/1 mullite dissolution devoid of the accompanying effects of growing α-alumina platelets. Upon reactive wetting mullite dissolution gave rise to the formation of a broad cusp-like feature protruding along [0 1 0] into the substrate. Its trailing edges were approximately parallel to {1 3 0} mullite. Note that typically the mullite dissolution path driven by a fast growing

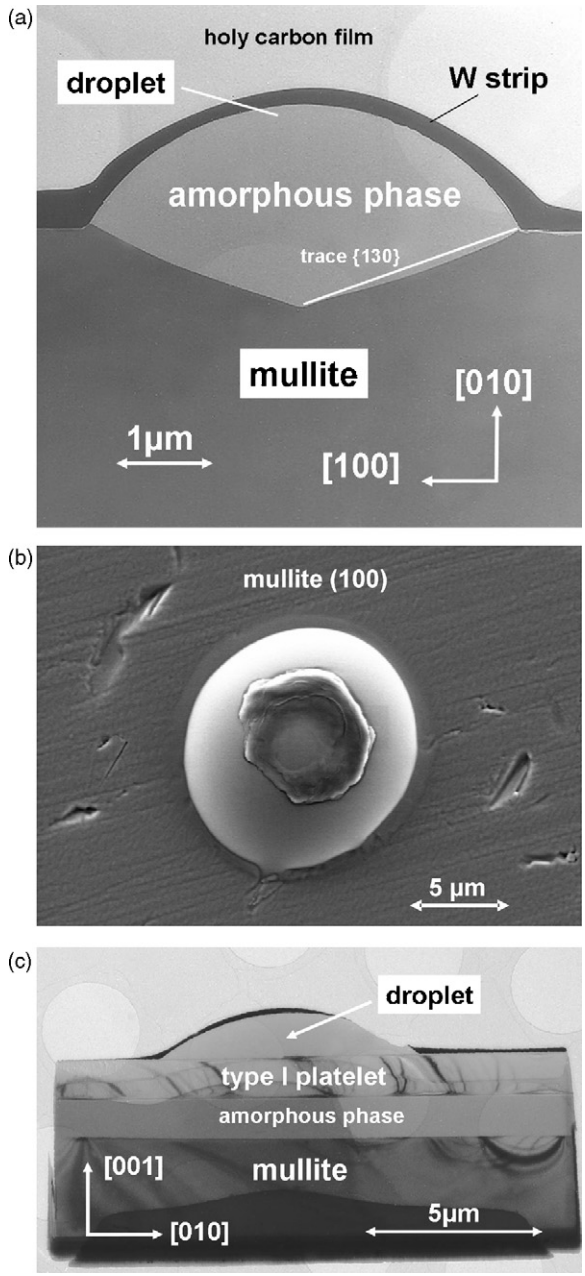

Fig. 10. (a) FIB section across a droplet deposited on (0 1 0) mullite upon annealing at 1400 °C/4 h (TEM, BF). Note cusp formation of the glass/mullite interface due to reactive wetting. Trailing edges of cusp are approximately parallel to {1 3 0}. (b) Droplet deposited on (1 0 0) mullite bottom surface holding a carbonaceous secondary phase particle upon quenching from 1400 °C annealing experiment (SE image). (c) FIB section across a droplet deposited on a type I α-alumina platelet (mullite (0 0 1) substrate, TEM, BF). Contrary to deposition on a mullite substrate (a) no reactive wetting is observed in this case.

α-alumina platelet (see Figs. 5 and 7) defined a much more narrow feature as compared to reactive wetting by a droplet. In contrast, for droplets laid down on α-alumina platelets no reactive wetting was observed resulting in lower Al_2O_3 concentration in the droplet (Fig. 10c). This latter image also proved that the droplets were deposited after completion of platelet formation thus confirming their late-stage formation during cool-down from ambient temperatures.

3.4. The effects of high water partial pressures on the mullite/α-alumina intergrowth at 1650 °C

Due to their low gas flow rate (v∼3 cm/s) at p_{H_2O} = 20 KPa, P_{total} = 100 KPa, the wet annealing conditions of this study were considered rather moderate as compared to previous work on high-temperature corrosion of polycrystalline mullite and alumina-rich ceramics in the presence of high gas velocities (v∼100 m/s) and high water partial pressures.[19–22] Naturally the silicon-rich glassy phase is prone to the effects of wet corrosion, however, the amount of corrosion damage imposed on the glassy phase was found to be clearly related to the specific orientation type of the α-alumina platelet.

For the type I α-alumina platelet situation, the thin amorphous interlayers connected to the surface of the specimen showed dewetting due to $Si(OH)_4$ evaporation (Fig. 3d). However, the majority of glassy phase located underneath a type I α-alumina platelet was effectively protected from high-temperature decomposition. For the same argument the glass layers surrounding the edge-on type II and the inclined type III α-alumina platelets (see Figs. 6b and 7a) were more prone to corrosive attack giving rise to deep corrosion pits (∼5 μm) into the glassy phase.

As compared to standard dry annealing a unique result of our wet annealing experiments is displayed in Fig. 3a and e: A secondary mullite [0 0 1] rod has precipitated from the furnace atmosphere on a type I α-alumina platelet. Notably, the mullite rod and the mullite (0 1 0) substrate share the same orientation relationship with the type I platelet (see Fig. 3c). For an open system characterized by a more turbulent gas flow during wet corrosion the steady removal of $Si(OH)_4$ and $Al(OH)_3$ from the mullite surface would render similar mullite reprecipitation impossible. In terms of the platelet formation process and the valid orientation relationships, no differences were found between dry and moderate wet annealing of 2/1 mullite.

4. Discussion

Alumina-on-mullite orientation relationships are best conceived by the observation that pronounced mullite dissolution paths were enforced by fast α-alumina platelet growth along densely packed mullite planes. These preferred mullite planes were parallel to {0 0·1}of α-alumina and therefore represent the characteristic mullite planes participating in the prevalent α-alumina/mullite orientation relationships (see Table 2). The significance of these mullite planes was further corroborated by the fact that they participated in the "snap-in conditions" (Fig. 8a) restricting the azimutal rotation of the α-alumina platelets around [0 0·1].

Orientation relationships between mullite and α-alumina were reported by Iwai et al.[16] and Saalfeld and Guse[17] under dry atmosphere and by Schmücker et al.[18] in wet atmosphere, respectively. No attempt was made in previous works to discriminate the different types of α-alumina platelet orientations or to discuss the functionality of a glassy phase coming with them. Iwai et al.[16] described the in-situ decomposition of a mullite microcrystal from an electro-cast mullite brick at 1750 °C with an initial composition between 3/2 and 2/1 mullite

($3.5Al_2O_3{\cdot}2SiO_2$, $x = 0.33$) followed by α-alumina formation. Assuming silica volatilization as the prevalent decomposition mechanism these authors evaluated three orientation relationships between mullite and the newly formed α-alumina using classical Weissenberg X-ray techniques. Their data involving the (1 1 0), (1 3 0), and (3 1 0) mullite planes correspond to orientation relationships determined in this study from type II α-alumina platelets on (0 0 1) mullite as well as type II and III platelets on (1 0 0) and (0 1 0) mullite (Table 2).

Saalfeld and Guse[17] analyzed the phase formation upon solidification of an Al_2O_3–SiO_2 melt close to the eutectic point located at $T_e = 1889.5\,^{\circ}C$; 77.9 wt% Al_2O_3, 22.1 wt% SiO_2 with $x_e = 0.418$, according to the SiO_2–Al_2O_3 phase diagram refined by Eriksson and Pelton.[9] They reported two orientation relationships involving the (1 0 0) mullite plane which are confirmed by our data derived from type I α-alumina platelets on (1 0 0) mullite and type II platelets on (0 1 0) mullite, respectively.

The two orientation relationships reported by Schmücker et al.[18] from hydroxylated (0 0 1) and (0 1 0) single crystal 2/1 mullite sections are consistent with our data derived from type I platelets on (0 1 0) mullite.

Structural constraints supporting topotactic orientation relationships during α-alumina on mullite intergrowth have been first addressed by Iwai et al.[16] The common argument emphasized the similarity in the structural arrangement of oxygen anions between (i) the {3 1 0} mullite planes and (ii) the hexagonal-close-packed (0 0·1) plane in the α-alumina structure. These authors concluded that upon thermal decomposition of mullite the {3 1 0} plane would be almost preserved when converted into the (0 0·1) α-alumina plane.

The same orientation relation, namely (0 0·1)//($\bar{3}$ 1 0) in our notation, was experimentally confirmed during TEM inspection of a type III platelet on (0 0 1) mullite (cf. Table 2 and Fig. 7a). The corresponding diffraction pattern (Fig. 7b) revealed a α-alumina/mullite pair of parallel lattice planes 1 1·0//1 3 0 which match in *d*-spacings within <2% ($d_{1\,1{\cdot}0} = 0.2379$ nm versus $d_{1\,3\,0} = 0.2427$ nm). These close-matching planes extend perpendicular across (0 0·1)//($\bar{3}$ 1 0), thus qualifying this interface as a composition plane during α-alumina nucleation on mullite. Likewise, for a type I platelet on (0 0 1) mullite, i.e. (0 0·1)//(0 0 1), electron diffraction (Fig. 2b) identified the pair of parallel lattice planes $0\,\bar{3}\cdot 0$//$\bar{4}\,\bar{4}\,0$ which exhibit close matching *d*-values ($d_{0\,\bar{3}{\cdot}0} = 0.1374$ nm versus $d_{\bar{4}\,\bar{4}\,0} = 0.1346$ nm) and continue perpendicular across the composition plane (see also Fig. 11a). Note that in both cases the lattice planes parallel to the composition planes, i.e. 0 0·6//$\bar{3}$ 1 0(Fig. 7b) and 0 0·6 //0 0 1 (Fig. 2b), differ significantly in *d*-spacings thus emphasizing the significance of lattice planes extending perpendicular to mutual composition planes.

The *cation* sublattices of α-alumina and mullite provide ideal reference systems for visualizing the alumina-on-mullite intergrowth in real space. Unlike the complex *anion* sublattices this approach offers a more transparent perspective of α-alumina/mullite orientation relationships utilizing the fact that continuity of numerous lattice planes densely packed with aluminum atoms can be verified between constituents (Fig. 11a and b). In the mullite cation sublattice the fully occupied octahedral Al position, the disordered T position with (Si, Al) site occupancy ~0.8 and the disordered T* position with (Si, Al) site occupancy ~0.2 have to be distinguished,[13,14] while in α-alumina fully occupied Al positions are considered only.

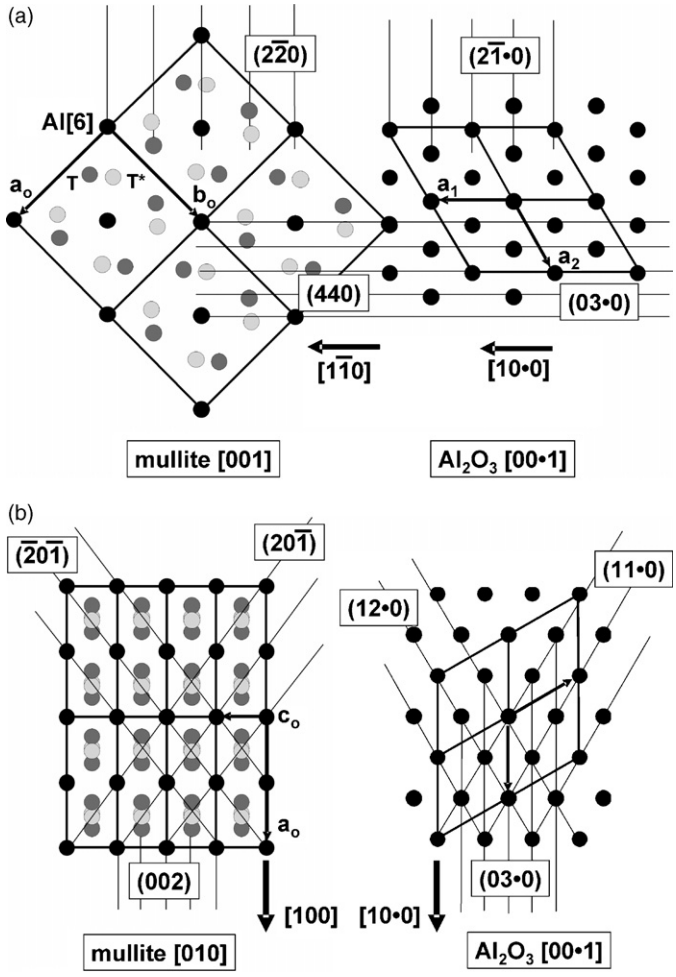

Fig. 11. (a) Visualizing the continuity of cation sublattices (2 × 2 cells) in α-alumina/mullite orientation relationships in real space: type I α-alumina (0 0·1) platelet on mullite (0 0 1) defined by the snap-in condition [1 $\bar{1}$ 0]//[1 0·0]. Relevant Al-positions include the fully occupied octahedral Al position (bold dots), the disordered T position with (Si, Al) site occupancy ~0.8 (dark gray dots) and the disordered T* position with (Si, Al) site occupancy ~0.2 (light gray dots). Note perfect alignment of lattice planes (0 3·0)//(4 4 0) and (2 $\bar{1}$ · 0)//(2 $\bar{2}$ 0) across the possible composition plane parallel to (0 0·1)//(0 0 1), with very good and reasonable matching of the *d*-spacings, respectively. (b) Visualizing the continuity of cation sublattices in α-alumina/mullite orientation relationships in real space: type I-alumina (0 0·1) platelet on mullite (0 1 0) defined by the snap-in condition [1 0 0]//[1 0·0]. For cation site occupancies see (a).

One example of a α-alumina (0 0·1) platelet on (0 0 1) mullite is displayed in Fig. 11a. For the snap-in condition [1 0·0]//[1 $\bar{1}$ 0] continuity of the (0 3·0) versus (4 4 0) lattice planes is obvious. Note that these planes were verified as perfectly matching planes across the composition plane (cf. Fig. 2b). The (2 $\bar{1}$ · 0) and (2$\bar{2}$0) planes are well aligned but differ in *d*-spacing by approximately 12%. Additional matching planes were omitted for the sake of simplicity. In a second example (Fig. 11b), matching planes in both cation sublattices comprised symmetry-equivalent planes in α-alumina and mullite as shown for a

α-alumina (0 0·1) platelet on mullite (0 1 0) defined by the snap-in condition [1 0·0]//[1 0 0]. The densely packed Al-rows in both constituents extending parallel to (0 3·0) and (0 0 2) match very well. The $\{1\,1{\cdot}0\}$ versus $\{2\,0\,\bar{1}\}$ lattice planes match fairly close in *d*-spacing but require an additional 6° tilt in order to achieve perfect alignment of planes. Similar small angular deviations are not uncommon for topotactic orientation relationships in ceramic systems.

The structural similarites between both cation sublattices, visualized here for two examples, confirm that α-alumina/mullite orientation relationships are supported by a high degree of coherency across the experimentally observed interfaces. For the same argument the boundary condition for platelet growth, that is minimizing the deformation energy per volume was fulfilled. However, once α-alumina nucleated and the growing platelet was completely wetted by the glassy phase, the lack of any stress birefringence patterns at the α-alumina/mullite interfaces indicated that the boundary criterion now relaxed thus allowing free growth of α-alumina platelet in any direction.

The glassy phase played a key role during platelet growth and therefore its prevalent phase relationships were addressed in more detail. Firstly, it should be noted that the Al_2O_3 content of the glassy phase was not far from that of the eutectic liquid (approximately 18 wt% Al_2O_3 at $T_e \sim 1260\,^{\circ}C$) in the *metastable* SiO_2–Al_2O_3 phase diagram,[32] that is in the absence of any mullite phase, which was determined from firing of cristobalite–80 wt% alumina compacts at subsolidus temperatures. Secondly, the surprisingly high aspect ratio of the (0 0·1) α-alumina platelets of about 1:60 indicated that the glassy phase has acted as a build-in flux during platelet growth. Since pure silica glass formed according to Eq. (2) is a poor flux due to its high viscosity, the glassy phase experienced a major composition/viscosity adjustment via uptake of network modifying cations, and thereby allowed enhanced Al-diffusion from the mullite dissolution sites through the glass network to the growth front of the α-alumina platelets.

Due to the dominance of sodium in comparison to the other impurities the glassy phase may be reduced to a constituent of the ternary system Na_2O–SiO_2–Al_2O_3.[33] The bulk composition (Section 3.3) plotted into the compatibility triangle silica-albite $NaAlSi_3O_8$-mullite[34] and layed in the primary mullite field next to the binary eutectic line silica-mullite. Interestingly, the bulk composition was also very close to the binary invariant point I with 8.1 wt% Na_2O, 13.3% Al_2O_3, 78.6% SiO_2, located along the join silica-$Na_2O{\cdot}Al_2O_3$ at 1050 °C.[33] Under equilibrium conditions the melt would react at point I with mullite to form albite and tridymite, but in our case it persisted metastable as a quenched glass. Looking at our glassy phase as a similar melt (molar ratio $Na_2O/Al_2O_3 = 1$) finds Al^{3+} acting as a network modifier in a fully polymerized network while charge-balanced with Na^+. Both ions are tetrahedrally coordinated.[35–37]

The morphology of platelets grown from the glassy phase is characterized by special forms of the trigonal class $\bar{3}2/m1$ only. This is very similar to sapphire grown from molten cryolite fluxes.[38,39] Notably, the alumina content of cryolite fluxes ($\geq$10 wt% Al_2O_3) is of the same order as the glassy phase surrounding the platelets.[40] Fast growth normal to the *c*-axis and slow growth parallel to the *c*-axis results in highly anisotropic growth characteristics of the α-alumina platelets dominated by the basic pinacoid $c\,\{0\,0{\cdot}1\}$ as the largest and therefore the slowest growing face. Besides the pinacoid, terminating faces of the α-alumina platelets include the rhombohedral face $r\,\{0\,h{\cdot}l\}$ and the hexagonal bipyramid face $p\,\{h\,h{\cdot}l\}$ in agreement with the α-alumina Wulff equilibrium shape.[41]

Our annealing experiments (Section 3.2) showed that the glassy phase could not have achieved its functionality without the doping effects of external impurity sources modifying its bulk composition. While the Al/Si ratio in the glassy phase is primarily determined by mullite dissolution, the other network modifying cations (Na, Mg, Ca) were definitely supplied by the kiln furnace material, most likely transported via alkali and alkaline earth vapor species to the α-alumina nucleation sites.

Kiln furniture materials, even considered high-purity, are known as notorious impurity sources in the refractory and furnace construction community[42,43] and numerous studies including the classic Johnson and Coble[44] experiment showed that vapor phase transport is a very effective way for doping of ceramic systems.[45,46] Along this line, Opila[29] pointed out that in wet oxidation experiments ($P_{H_2O} = 10$ KPa, 1200–1400 °C) some 100 ppm sodium and aluminum impurities from Al_2O_3 rods and hangers employed were sufficient to effect scale formation and oxidation rates of SiC. Nevertheless, the difficulties to separate *water vapor effects* from *impurity effects* prevailed[29] and also need to be addressed in the mullite system.

In the wet system nucleation and growth of α-alumina platelets were already accomplished *prior* to corrosion of the glassy phase via $Si(OH)_4$ evaporation. And even then, the amount of corrosive damage imposed on the glassy phase was dependent on the type of α-alumina platelet with type I platelets furnishing a protective shield for the underlying amorphous phase.

Among the metastable nature of 2/1 mullite upon annealing in the two-phase field "mullite plus alumina", the alumina platelet formation process relies on the effects of very specific impurity sources. In *qualitative* terms it appears of secondary importance whether these sources were eventually furnished by the combined effects of a (i) furnace atmosphere and the alumina kiln furniture (*dry annealing*) or (ii) by a gentle flowing water vapor stream leaching impurities (Na, Mg, Ca) from an alumina reaction tube (*wet annealing*). Leaving aside the subsequent effect of corrosive damage of the glassy phase, it is therefore not surprising that the same α-alumina-on-mullite microstructures resulted for both, dry and moderate wet annealing of 2/1 mullite. Consequently, rather than described by a *single-step* process (Eq. (2)), water vapor corrosion of single-crystal 2/1 mullite is better rationalized by a *two-step* process characterized by (i) mullite decomposition as the necessary silica forming step (Eq. (1)) followed by (ii) the actual corrosion of the glassy phase via silica volatilization.

This statement is true for our moderate water pressures ($P_{H_2O} = 0.2P_{total}$) and low gas velocities (3 cm/s) out to a couple of hours exposure time where the mullite decomposition rate, or rather the silica formation rate, clearly exceeded the silica

volatilization rate. Recently Schmücker et al.[18] claimed that no glassy phase did contribute to the formation of type I α-alumina platelets in their hydroxylation experiment of 2/1 single crystal mullite at 1200 °C/3 h, $P_{H_2O} = P_{total}$, $v \sim 10$ m/s. However, no microstructural evidence was provided. The two alumina-on-mullite orientation relationships they reported are consistent with our data (Table 2), suggesting that fundamentally different alumina-on-mullite microstructures did not emerge from their corrosion experiments as compared to this work. One may indeed question as to whether wet corrosion could ever drive an open 2/1 single crystal mullite system to release similar topotactically grown α-alumina platelets without the formation and functionality of the glassy phase. Its complete loss at a very early stage of hydroxylation would require remarkable SiO_2 volatilization rates which are only to be expected if high gas velocities *and* high water partial pressures work together.[4] Additional corrosion experiments are currently underway to shed light on this issue.

Finally it should be pointed out that the phenomena of oriented α-alumina platelet growth on annealed 2/1 mullite surfaces has been recognized in a variety of other high-temperature experiments which have been conducted independently at temperatures up to 1600 °C in either dry argon/helium purge gas or in dry air for different periods of time. These include (i) differential scanning calorimeter (DSC) experiments in order to determine the heat capacity of mullite[47], (ii) dilatometer and resonant ultrasound spectroscopy (RUS) experiments for determination of elastic properties of mullite[48], and (iii) sessile drop experiments for reactive wetting studies of mullite.[49] This is an interesting finding considering the fact that different furnaces and experimental setups were involved in these experiments. Moreover, one may assume that during numerous other high-temperature experiments involving 2/1 and 3/2 mullites the tiny clusters of α-alumina platelets formed on the mullite surface are left undetected upon routine inspection. Alumina sample holders as well as α-alumina clamping and fixture devices of different purity and design seem to represent the common denominator to all these experiments indicating that impurity doping via the vapor phase[29,42,43] does play a similar decisive role as discussed in this work.

5. Conclusions

Topotactic orientation relationships between α-alumina (0 0 0·1) platelets and Czochralski grown 2/1 mullite substrates were discussed in the light of annealing experiments of 2/1 mullite (0 0 1), (0 1 0), and (0 0 1) single crystals sections in the two-phase regime "mullite plus α-alumina" (1200–1650 °C) in different atmospheres (dry versus wet air) at normal air pressure.

Thermal decomposition of 2/1 mullite gave rise to the simultaneous formation of α-alumina platelets and an initially siliceous glassy phase completely wetting the platelets. Incorporation of networkmodifying cations (Na, Mg, Ca) from external impurity sources, i.e. (i) the kiln furniture material (*dry annealing*) and (ii) the alumina reaction tubes/fixtures (*wet annealing*), via vapor phase transport reduced the viscosity of the glassy phase as to provide a build-in flux for enhanced α-alumina platelet growth. Platelet aspect ratios of around 1:60 were observed. Upon nucleation on the mullite surfaces, fast growth of α-alumina platelet enforced pronounced mullite dissolution paths parallel to densely packed mullite planes.

The composition of the initially silica-rich glass in 2/1 mullite is found in agreement with the eutectic composition in the metastable Al_2O_3–SiO_2 system. Phase relationships of the modified glass upon uptake of impurities are rationalized in the ternary system Na_2O–Al_2O_3–SiO_2.

The growth habit of the α-alumina platelets is similar to that of sapphire from molten fluxes and is in agreement with the Wulff-shape of α-alumina. Growth faces correspond only to special forms of the trigonal point group $\bar{3}2/m$ including the c {0 0 0·1} pinacoid, the p {1 1 0·3} hexagonal bipyramid, and the r {0 1 0·2} rhombohedron. No hexagonal prisms a {1 1 0·0} or m {1 0 0·0} were developed. No twinning of platelets was observed.

Three different types of α-alumina platelets were formally distinguished: (i) the type I oriented parallel, (ii) the type II oriented perpendicular, and (iii) the type III inclined to the mullite surfaces (1 0 0), (0 1 0), and (0 0 1). Type II and III platelets were not independent from each other. The azimutual rotation of the platelets around [0 0 0·1] was restricted to specific snap-in conditons defined by specific mullite directions being parallel to the α-alumina a_1-axis: i.e. for type I platelets on (0 0 1) mullite substrate five symmetric non-equivalent orientation states were identified while the (1 0 0) and (0 1 0) mullite sections resulted in two orientation states, respectively.

The topotactic α-alumina/mullite orientation relationships were derived by OM, XRD, and FIB assisted TEM including previous work as a sub-assembly group (cf. Table 2). Mutual α-alumina/mullite lattice planes extending across possible composition planes during α-alumina nucleation on mullite were identified and rationalized in terms of coherency of cation sublattices.

The nature of the atmosphere (*dry versus moderate wet annealing*) had no effect to alumina-on-mullite intergrowth and the prevalent orientation relationships. Due to the low gas velocity and water vapor pressure employed during wet annealing, the silica formation rate controlled by mullite decomposition was always higher than the silica volatilization rate. Thus, platelet formation was accomplished before hot corrosion could set in indicating that hot corrosion of 2/1 mullite is best described by a two-step process. Corrosive damage imposed on the glassy phase was far less for type I α-alumina platelets as compared to type II and III platelets.

Oriented growth of α-alumina platelets on single crystal 2/1 mullite is enhanced by impurity doping of the coexisting glassy phase via vapor phase transport and represents a frequently observed feature during numerous other high temperature experiments employing 2/1 mullite single crystals.

Acknowledgements

The wet annealed 2/1 mullite specimens were supplied by Prof. S. Shimada, Hokkaido University, Sapporo, Japan, who

is gratefully acknowledged. The fruitful discussions with Prof. H.J. Kleebe, Technical University Darmstadt, Germany were very much appreciated.

References

1. Aksay, I. A., Dabbs, D. M. and Sarikaya, M., Mullite for structural, electronic, and optical applications. *J. Am. Ceram. Soc.*, 1991, **74**(10), 2343–2358.
2. Schneider, H. and Komarneni, S., ed., *Mullite*. Wiley-VCH, Weinheim, 2005.
3. Jacobson, N. S., Corrosion of silicon-based ceramics in combustion environments. *J. Am. Ceram. Soc.*, 1993, **76**(1), 3–28.
4. Opila, E. J., Oxidation and volatilization of silica formers in water vapor. *J. Am. Ceram. Soc.*, 2003, **86**(8), 1238–1248.
5. Davis, R. F., Aksay, I. A. and Pask, J. A., Decomposition of mullite. *J. Am. Ceram. Soc.*, 1972, **55**(10), 98–101.
6. Kroenert, W. and Buhl, H., The influence of various gaseous atmospheres on the melting behavior of mullite (Part I). *Interceram*, 1978, **1**, 68–72.
7. Kroenert, W. and Buhl, H., The Influence of various gaseous atmospheres on refractories in the system Al_2O_3-SiO_2 (Part II). *Interceram*, 1978, **2**, 140–146.
8. Xiao, Z. and Mitchell, B. S., Mullite decomposition kinetics and melt stabilization in the temperature range 1900–2000 °C. *J. Am. Ceram. Soc.*, 2000, **83**(4), 761–767.
9. Eriksson, G. and Pelton, A. D., Critical evaluation and optimization of the thermodynamic properties and phase diagrams of the CaO-Al_2O_3, Al_2O_3-SiO_2, and CaO-Al_2O_3-SiO_2 systems. *Metall. Trans. B*, 1993, **24B**, 807–816.
10. Bernal, J. D. and Mackay, A. L., Topotaxy. *Mineral. Petrol.*, 1965, **10**, 331–340.
11. Kleebe, H. J., Siegelin, F., Straubinger, T. and Ziegler, G., Conversion of Al_2O_3-SiO_2 powder mixtures to 3:2 mullite following the stable or metastable phase diagram. *J. Eur. Ceram. Soc.*, 2001, **21**, 2521–2533.
12. Sadanaga, R., Tokonami, M. and Takeuchi, Y., The structure of mullite, $2Al_2O_3{\cdot}SiO_2$, and relationship with the structures of sillimanite and andalusite. *Acta Cryst.*, 1962, **15**, 65–68.
13. Saalfeld, H. and Guse, W., Structure refinement of 3:2-mullite ($3Al_2O_3{\cdot}2SiO_2$). *Neues Jahrb. Mineral. Monatsh.*, 1981, **4**, 145–150.
14. Angel, R. J. and Prewitt, C. T., Crystal structure of mullite: a re-examination of the average structure. *Am. Mineral.*, 1986, **71**, 1476–1482.
15. Lee, W. E. and Lagerlof, K. P. D., Structural and electron diffraction data of sapphire α-Al_2O_3. *J. Elect. Mic. Tech.*, 1985, **2**, 247–258.
16. Iwai, S.-I., Watanabe, T., Minato, I., Okada, K. and Morikawa, H., Decomposition of mullite by silica volatilization. *J. Am. Ceram. Soc.*, 1980, **63**(1–2), 44–46.
17. Saalfeld, H. and Guse, W., Mullite single crystal growth and characterization. In *Mullite and Mullite Composites*, *Vol. 6*, ed. S. Somiya, R. F. Davis and J. A. Pask. The American Ceramic Society, Westerville (OH), 1990, pp. 73–101.
18. Schmücker, M., Mechnich, P., Zaefferer, S. and Schneider, H., The high-temperature mullite/α-alumina conversion in rapidly flowing watervapor. *Scripta Mat.*, 2006, **55**, 1131–1134.
19. Jacobson, N. S., Fox, D. S., Smialek, J. L., Opila, E. J., Tortorelli, P. F., Moore, K. L., Nickel, K. G., Hirata, T., Yoshida, M. and Yuri, I., Corrosion issues for ceramics in gas turbines. In *Ceramic Gas Turbine Component Development and Characterization: Progress in Ceramic gas Turbine Development*, *Vol. 2*, ed. M. V. Roode, M. F. Ferber and D. W. Richerson. The American Society of Mechanical Engineers, 2003, pp. 607–640.
20. Yuri, L. and Hisamatsu, T., Recession rate prediction for ceramic materials in combustion gas flow. In *Proceedings of ASME Turbo Expo*, 2003, ASME Paper GT 2003-38886.
21. Klemm, H., Fritsch, M. and Schenk, B., Corrosion of ceramic materials in hot gas environments. *Ceram. Eng. Sci. Proc.*, 2004, **25**, 463–468.
22. Fritsch, M., Klemm, H., Hermann, M. and Schenk, B., Corrosion of selected ceramic materials in hot gas environment. *J. Eur. Ceram. Soc.*, 2006, **26**, 3557–3565.
23. Ueno, S., Jayaseelan, D. D., Kondo, N., Ohji, T. and Kanazai, S., Water vapor corrosion of mullite containing small amounts of sodium. *Ceram. Int.*, 2005, **31**, 177–180.
24. Rüscher, C. H., Shimada, S. and Schneider, H., High-temperature hydroxylation of mullite. *J. Am. Ceram. Soc.*, 2002, **85**(6), 1616–1618.
25. Eils, N., Rüscher, C. H., Shimada, S., Schmücker, M. and Schneider, H., High-temperature hydroxylation and surface corrosion of 2/1 mullite single crystals in water vapor environments. *J. Am. Ceram. Soc.*, 2006, **89**(9), 2887–2894.
26. Guse, W. and Mateika, D., Growth of mullite single crystals ($2Al_2O_3{\cdot}SiO_2$) by the Czochralski method. *J. Cryst. Growth*, 1974, **22**, 237–240.
27. Guse, W., Compositional analysis of czochralski grown mullite single crystals. *J. Cryst. Growth*, 1974, **26**, 151–152.
28. Bertram, R. and Klimm, D., Assay measurements of oxide materials by thermogravimetry and ICP-OES. *Thermochim. Acta*, 2004, **419**, 189–193.
29. Opila, E. J., Oxidation kinetics of chemically vapor-deposited silicon carbide in wet oxygen. *J. Am. Ceram. Soc.*, 1994, **77**(3), 730–736.
30. Rehak, P., Kunath-Fandrei, G., Losso, P., Hildmann, B., Schneider, H. and Jäger, C., Study of the Al coordination in mullites with varying Al:Si ratio by ^{27}Al NMR spectroscopy and X-ray diffraction. *Am. Mineral.*, 1998, **83**, 1266–1276.
31. Jackson, A. G., *Handbook of Crystallography*. Springer, New York, 1991.
32. Risbud, S. H. and Pask, J. A., SiO_2-Al_2O_3 metastable phase equilibrium diagram without mullite. *J. Mater. Sci.*, 1978, **13**, 2449–2454.
33. Schairer, J. F. and Bowen, N. L., Melting relations in the systems Na_2O-Al_2O_3-SiO_2 and K_2O-Al_2O_3-SiO_2. *Am. J. Sci.*, 1947, **245**, 193–204.
34. Jacobson, N. S. and Lee, K. N., Corrosion of mullite by molten salts. *J. Am. Ceram. Soc.*, 1996, **79**(8), 2161–2167.
35. Urbain, G., Bottinga, Y. and Richer, P., Viscosity of liquid silica, silicates and alumino-silicates. *Geochim. Cosmochim. Acta*, 1982, **46**, 1061–1072.
36. Toplis, M. J., Dingwell, D. B., Lenci, T. and Viscosity, Fragility and configurational entropy of melts along the join SiO_2-$NaAlSiO_4$. *Am. Mineral.*, 1997, **82**, 979–991.
37. Mysen, B. O. and Virgo, D., Structure and properties of fluorine-bearing aluminosilicate melts: the system Na_2O-Al_2O_3-SiO_2-F at 1 atm. *Contrib. Mineral. Petrol.*, 1985, **91**, 205–220.
38. Timofeeva, V. A. and Lukyanova, N. I., Solubility and conditions of growth of corundum from molten fluxes. *Soviet Phys.-Chrystallogr.*, 1967, **12**, 77–81.
39. Jang, J. W., Lee, T. K. and Chung, S. J., Crystal habits of corundum single crystals grown in cryolite flux. *J. Korean Ceram. Soc.*, 1992, **6**(6), 463–470.
40. Foster, P. A., Determination of the cryolite-alumina phase diagram by quenching methods. *J. Am. Ceram. Soc.*, 1960, **43**(2), 66–68.
41. Kitayama, M. and Glaeser, A. M., The wulff shape of alumina: III, undoped alumina. *J. Am. Ceram. Soc.*, 2002, **85**(3), 611–622.
42. Allendorf, M. D. and Spear, K. E., Thermodynamic analysis of silica refractory corrosion in glas furnaces. *J. Electrochem. Soc.*, 2000, **148**(12), B59–B67.
43. Beerkens, R. G. C. and Verheijen, O. S., Reactions of alkali vapors with silica based refractory in glass furnaces, thermodynamics and mass transfer. *Phys. Chem. Glasses*, 2005, **46**, 583–594.
44. Johnson, W. C. and Coble, R. L., A test of the second-phase and impurity segregation models for MgO-enhanced densification of sintered alumina. *J. Am. Ceram. Soc.*, 1978, **61**(3–4), 110–114.
45. Reaney, D. W., Vapor transport and sintering. In *Sintering of Advanced Ceramics, Ceramic Transactions*, *Vol. 7*, ed. C. A. Handwerker, J. E. Blendell and W. A. Kaysser. American Ceramic Society, Westerville, OH, 1990, pp. 86–110.
46. Simpson, Y. K. and Carter, C. B., Faceting behavior of alumina in the presence of a glass. *J. Am. Ceram. Soc.*, 1990, **73**(8), 2391–2398.

47. Hildmann, B. and Schneider, H., Heat capacity of mullite: new data and evidence for a high-temperature phase transformation. *J. Am. Ceram. Soc.*, 2004, **87**(2), 227–234.
48. Schreuer, J., Hildmann, B. and Schneider, H., Elastic properties of mullite single crystals up to 1400 °C. *J. Am. Ceram. Soc.*, 2006, **89**(5), 1624–1631.
49. Braue, W., Hildmann, B., Schneider, H., Eldred, B. T. and Ownby, P. D., Reactive wetting of mullite $Al_2[Al_{2+2x}\ Si_{2-2x}]O_{10-x}$ single crystals by yttrium-aluminosilicate and borosilicate glasses. *J. Mater. Sci.*, 2005, **40**(9/10), 2335–2340.